

QSO ABSORPTION SYSTEMS DETECTED IN NE VIII: HIGH-METALLICITY CLOUDS WITH A LARGE EFFECTIVE CROSS SECTION¹

J.D. MEIRING², T. M. TRIPP², J. K. WERK³, J.C. HOWK⁴, E.B. JENKINS⁵, J. X. PROCHASKA³, N. LEHNER⁶, K. R. SEMBACH⁶

Draft version November 1, 2018

ABSTRACT

Using high resolution, high signal-to-noise ultraviolet spectra of the $z_{\text{em}}=0.9754$ quasar PG1148+549 obtained with the Cosmic Origins Spectrograph (COS) on the *Hubble Space Telescope*, we study the physical conditions and abundances of Ne VIII+O VI absorption line systems at $z_{\text{abs}}=0.68381, 0.70152, 0.72478$. In addition to Ne VIII and O VI, absorption lines from multiple ionization stages of oxygen (O II, O III, O IV) are detected and are well-aligned with the more highly ionized species. We show that these absorbers are multiphase systems including hot gas ($T \approx 10^{5.7}$ K) that produces Ne VIII and O VI, and the gas metallicity of the cool phase ranges from $Z = 0.3Z_{\odot}$ to supersolar. The cool ($\approx 10^4$ K) phases have densities $n_H \approx 10^{-4}$ cm⁻³ and small sizes (< 4 kpc); these cool clouds are likely to expand and dissipate, and the Ne VIII may be within a transition layer between the cool gas and a surrounding, much hotter medium. The Ne VIII redshift density, $dN/dz \sim 7_{-3}^{+7}$, requires a large number of these clouds for every $L > 0.1L^*$ galaxy and a large effective absorption cross section ($\gtrsim 100$ kpc), and indeed, we find a star forming $\sim L^*$ galaxy at the redshift of the $z_{\text{abs}}=0.72478$ system, at an impact parameter of 217 kpc. Multiphase absorbers like these Ne VIII systems are likely to be an important reservoir of baryons and metals in the circumgalactic media of galaxies.

Subject headings: galaxies: halos — intergalactic medium — quasars: absorption lines — quasars: individual (PG1148+549)

1. INTRODUCTION

The cosmic baryon fraction is now well constrained to a value $f_b = 0.17 \pm 0.01$ by both the interpretation of deuterium abundances in the framework of big bang nucleosynthesis (O’Meara et al. 2006; Pettini & Cooke 2012) and observations of the cosmic microwave background (Spergel et al. 2007). In contrast, the contributions of readily observed stellar and gas components in nearby galaxies are far below this value (Persic & Salucci 1992; Fukugita et al. 1998; Bell et al. 2003). One explanation for the “missing baryons” is that substantial quantities of low density gas reside in the intergalactic medium (IGM) or in the halos of galaxies and groups (now generally referred to as the “circumgalactic” medium, CGM), and this matter is heated during infall into the dark matter potential wells that surround the visible galaxies (Davé et al. 2001; Cen & Fang 2006; Tepper-García et al. 2011; Smith et al. 2011). This shock heating is a universal prediction of hydrodynamical simulations of structure formation, and it is expected to transform the gas from cool ($\approx 10^4$ K) clouds that are straightforward to de-

tect (Rauch et al. 1997; Weinberg et al. 1997) into hotter phases ($10^5 - 10^7$ K) that are much more difficult to study. How the intergalactic gas is physically processed as it descends into galaxies has important implications for galaxy evolution (Kereš et al. 2005, 2009; Dekel & Birnboim 2006; Bouché et al. 2010). For example, it is possible that the some of the baryons cannot cool and fall into the star-forming disk (Maller & Bullock 2004) or are somehow prevented from entering galactic potential wells in the first place (Anderson & Bregman 2010). In any case, the observations indicate that the majority of the baryons in the Universe are not located in the disks of galaxies; rather, they are sequestered in highly ionized, low-density gas in galaxy halos and the intergalactic medium (IGM). Currently, the most sensitive method to study such low-density plasmas is to search for the ultraviolet (UV) absorption lines imprinted on the spectrum of a background quasistellar object (QSO) from foreground, low-density material.

In addition to probing the missing baryons, QSO absorption spectroscopy of the CGM of galaxies provides unique insights on the roles played by gas inflows and outflows in galaxy evolution. Simple closed-box models of galactic chemical evolution fail to reproduce the distribution of stellar metallicities in the Milky Way and nearby galaxies (e.g., van den Bergh 1962; Larson 1972; Tinsley 1975; Pagel & Edmonds 1981; Tosi 1988; Worthey et al. 1996). This well known “G-dwarf problem” indicates that galaxies continue to acquire gas from their intergalactic surroundings over much of their lifetimes. Exactly how this gas accretion occurs is an open question with important implications. In contrast to the traditional picture of hot accretion through a spherical accretion shock (e.g., White & Rees 1978), more recent

¹ Based on observations made with the NASA/ESA Hubble Space Telescope, obtained at the Space Telescope Science Institute, which is operated by the Association of Universities for Research in Astronomy, Inc., under NASA contract NAS 5-26555. These observations are associated with program GO11741.

² Department of Astronomy, University of Massachusetts, Amherst, MA 01003, USA

³ University of California Observatories-Lick Observatory, UC Santa Cruz, CA 95064, USA

⁴ Department of Physics, University of Notre Dame, 225 Nieuwland Science Hall, Notre Dame, IN 46556, USA

⁵ Princeton University Observatory, Peyton Hall, Ivy Lane, Princeton, NJ 08544, USA

⁶ Space Telescope Science Institute, 3700 San Martin Drive, Baltimore, MD 21218, USA

theoretical studies suggest that gas accretes in filamentary structures, and it may be able to cool as it accretes so that it never approaches the virial temperature (Kereš et al. 2005, 2009; Dekel & Birnboim 2006; Brooks et al. 2009; Fumagalli et al. 2011; Stewart et al. 2011). Signatures of this “cold” accretion are difficult to identify, but recent QSO absorption-line studies have provided some observational evidence of cold accretion (Tripp et al. 2005; Ribaldo et al. 2011; Giavalisco et al. 2011; Thom et al. 2011; Churchill et al. 2012; Kacprzak et al. 2012; Lehner et al. 2013). These investigations have revealed very low metallicity gas in the halos of high metallicity galaxies; this low metallicity material is generally cool and could arise in the accretion flows, which are expected to be metal-poor.

Similarly, simulations and analytical models of galaxy formation and evolution require massive *outflows* to account for the observed properties of galaxies such as the ISM metallicities and the mass-metallicity relation, total stellar masses, discrepancies in the galaxy luminosity function compared to expectations from cold-dark matter cosmology, and IGM enrichment (e.g., Dekel & Silk 1986; Springel & Hernquist 2003; Oppenheimer & Davé 2006). Feedback processes from current or recent star formation, either through radiatively driven or supernova-driven galactic-scale winds (or the combined effects of both processes, see Murray et al. 2011) are thought to play crucial roles in the evolution of a galaxy by injecting energy and mass into the CGM and beyond into the IGM. Such outflows are seen in nearby star forming galaxies (Heckman et al. 1995; Martin et al. 2002; Veilleux et al. 2005) and are ubiquitous in some types of higher-redshift galaxies (Tremonti et al. 2007; Weiner et al. 2009; Steidel et al. 2010), but most of these studies provide little or no information on the full spatial extent, total mass, and overall impact of the outflows (cf., Tripp et al. 2011), either because the source of the outflow is used as the continuum source (and thus the spatial extent of the flow is unconstrained) or because the studies have inadequate leverage on the ionization and metallicity of the gas.

Which QSO absorption lines provide constraints on the missing baryons and inflows/outflows? The O VI $\lambda\lambda$ 1031.9, 1037.6 lines arising from O⁵⁺, which has a peak ionization fraction at $\sim 300,000$ K in collisional ionization equilibrium (Gnat & Sternberg 2007), have been used to trace hot gas in a range of environments from the local ISM to the CGM/IGM (e.g., Jenkins 1978; Tripp et al. 2000; Chen & Prochaska 2000; Howk et al. 2002; Sembach et al. 2003; Savage & Lehner 2006; Stocke et al. 2006; Bowen et al. 2008; Wakker & Savage 2009; Chen & Mulchaey 2009; Howk et al. 2009; Lehner et al. 2009; Narayanan et al. 2012, and references therein). Recent observations indicate that the extended halos of star forming galaxies are filled with highly ionized and metal-enriched gas traced by O VI, and a large fraction of star-forming galaxies have detectable O VI absorption in their halos out to impact parameter $\rho \approx 150$ kpc (Tumlinson et al. 2011b). Absorption by O VI is also detected in the halos of early-type galaxies, but less frequently (Tumlinson et al. 2011b), while strong H I absorption is ubiquitous in galaxy halos at $\rho \lesssim 150$ kpc regardless of galaxy type (Thom et al. 2012). This circumgalactic ma-

terial appears to contain a substantial amount of mass, comparable to the mass of the ISM in the galaxy itself (Tumlinson et al. 2011b; Tripp et al. 2011; Prochaska et al. 2011).

However, the physical nature of the O VI-bearing gas (e.g., collisionally ionized vs. photoionized) is a debated and open question (Tripp et al. 2008), a question with important ramifications. Hydrodynamical simulations of galaxy evolution show that O VI absorbers typically reside in metal enriched regions with overdensities $\rho/\langle\rho\rangle = 1-100$ (Cen et al. 2001; Fang & Bryan 2001; Cen & Fang 2006; Davé et al. 2001; Tepper-García et al. 2011; Oppenheimer & Davé 2009; Cen & Chisari 2011; Oppenheimer et al. 2011; Smith et al. 2011), and these models have made detailed predictions regarding the strength and physical nature of O VI absorbers as a function of impact parameter and galaxy luminosity (Ganguly et al. 2008; Cen & Chisari 2011; Stinson et al. 2012; Brady Ford et al. 2012). Simulations by Tepper-García et al. (2011) indicate that O VI does appear to trace primarily shock heated gas, with the distribution of temperatures peaked at $\sim 10^{5.3}$ K. However, ~ 30 percent of the O VI systems in that simulation are at lower temperatures and are *primarily* photoionized by the ultraviolet background flux. Other simulations indicate that O VI and even Ne VIII absorbers⁷ arise primarily in photoionized gas (Oppenheimer & Davé 2009; Oppenheimer et al. 2011). Interestingly, $\sim 30\%$ of the *observed* O VI absorbers have characteristics of cool, photoionized gas (Tripp et al. 2008).

Despite recent advances in the UV absorption spectroscopy of the low- z IGM, several questions are still unanswered, due in part to the lack of adequate diagnostic lines at low redshift. The baryonic content, metallicity, and ionization mechanisms of the gas comprising the IGM and CGM are only loosely constrained, and the roles played by circumgalactic and intergalactic gases in galaxy evolution are still highly uncertain. Much of the work on low- z absorption lines has been accomplished with the *Hubble Space Telescope* Space Telescope Imaging Spectrograph (STIS) and *Far Ultraviolet Spectroscopic Explorer* (FUSE); these spectrographs can only study the brightest QSOs in reasonable exposure times. At the redshifts of the absorbers that have typically been studied with STIS and *FUSE*, only a limited set of absorption lines is available for analysis, and much of the determination of the physical conditions in the systems is based on H I and O VI alone, or on column density ratios of different ions such as C III, Si III, and O VI. Consequently, there can be degeneracies between effects due to ionization, non-solar relative abundances, and depletion by dust. Moreover, with a limited set of transitions, key species in the analysis (e.g., C III and Si III, which have only one strong resonance transition at $\lambda > 912$ Å) are prone to saturation.

In order to overcome some of these issues and to better constrain the physical conditions in the IGM and CGM, we have undertaken a blind survey of $z \sim 1$ QSOs with

⁷ We note, however, that most of the Ne VIII absorbers predicted by Oppenheimer et al. (2011) have Ne VIII column densities that are much lower than the observed Ne VIII column densities that have been reported thus far; the stronger Ne VIII systems that have been observed are likely to originate in collisionally ionized gas in the simulations of Oppenheimer et al. (2011).

the COS spectrograph (Froning & Green 2009; Green et al. 2012). At moderate redshifts, we can access many of the numerous absorption lines in the FUV at $\lambda_{\text{rest}} < 912 \text{ \AA}$ (Verner et al. 1994), which provides several advantages compared to previous studies: First, multiple and adjacent ionization states of oxygen as well as many other ions (e.g., O I – O VI, N I – N V, S II – S VI, etc.) are available at $\lambda \gtrsim 600 \text{ \AA}$ in the rest frame so that diagnostics of physical conditions ranging from $T \approx 10^3 \text{ K}$ up to $T \gg 10^5 \text{ K}$ can be exploited without confusion from assumptions about the relative abundances of the elements. Likewise, relative abundances can be constrained with the ambiguity from ionization corrections greatly reduced. Finally, in this wavelength range, many species have multiple transitions so that if a strong line is saturated or a line is badly affected by blending, other transitions can still be used to measure the column density of interest. At $z \sim 0.5$, these transitions enter the bandpass of the Cosmic Origins Spectrograph (COS) onboard the *Hubble Space Telescope* (HST).

Aside from O VI, other highly ionized species have resonance transitions that are accessible in the FUV. For example, the Ne VIII $\lambda\lambda 770,780$ doublet enters the COS bandpass at $z \gtrsim 0.45$. In diffuse halo gas or the intergalactic medium, it is difficult to photoionize neon up to Ne VIII: the ionization potential of Ne VII is 207 eV and the ionization potential of Ne VIII is 239 eV. Neither stars nor background quasars produce an ionizing flux field with many photons at these energies (cf. Fox et al. 2005; Haardt & Madau 2012), and photoionization models typically require very low densities and, in turn, very large clouds to yield detectable quantities of Ne VIII (Savage et al. 2005; Narayanan et al. 2011). While Ne VIII is difficult to produce by photoionization, it can easily originate via collisional ionization in gas that is sufficiently hot. Consequently, Ne VIII is expected to be an unambiguous indicator of collisionally ionized hot gas. Several intervening⁸ absorption systems bearing Ne VIII have been discovered, indicating highly ionized and multiphase gas with temperatures of $T=10^5 - 10^6 \text{ K}$ in the hot material (Savage et al. 2005; Tripp et al. 2011; Narayanan et al. 2011, 2012).

The excellent sensitivity of COS in the UV provides an opportunity to study the IGM and CGM in much more detail than has been achievable in the past. Using our high signal-to-noise COS spectrum of the QSO PG1148+549, in this paper we study in detail absorption systems at $z \sim 0.7$ where we have access to a number of ionization states of oxygen (O I to O VI) and the Ne VIII $\lambda\lambda 770, 780$ doublet; we also place limits on other banks of (undetected) adjacent ions such as the sulfur ions. We will show that the O VI and Ne VIII does indeed arise in plasma with $T \gg 10^5 \text{ K}$, but this hot gas has an intimate relationship with lower ionization material – the hot gas likely originates in some sort of interface on the surface of the cooler, low-ionization clouds (e.g., Kwak

⁸ The Ne VIII doublet has also been detected in a number of “proximate” absorbers with $z_{\text{abs}} \approx z_{\text{QSO}}$ (e.g., Petitjean & Srianand 1999; Ganguly et al. 2006; Muzahid et al. 2012, 2013); these proximate absorbers show evidence that they are close to the central engine of the QSO and thus probe a different aspect of galaxies than the intervening systems. In this paper, we are primarily interested in diffuse gas in the halos of galaxies and the IGM, so we do not include the proximate systems in our discussions.

Table 1
Cosmic Origins Spectrograph Observations of PG1148+549

COS Grating	λ_{cen} (\AA)	Observation Date	Exposure Time (seconds)	MAST ID ^a
G130M	1309	2009 Dec. 30	3192	LB1O22Q3Q
G130M	1309	2009 Dec. 30	3192	LB1O22RAQ
G130M	1309	2009 Dec. 30	2527	LB1O22PMQ
G130M	1327	2009 Dec. 26	2527	LB1O23EBQ
G130M	1327	2009 Dec. 30	3192	LB1O22RHQ
G130M	1327	2009 Dec. 30	3192	LB1O22RRQ
G160M	1600	2009 Dec. 26	3192	LB1O23EOQ
G160M	1600	2009 Dec. 26	3192	LB1O23EFQ
G160M	1600	2009 Dec. 26	3192	LB1O23EVQ
G160M	1623	2009 Dec. 25	2482	LB1O24ACQ
G160M	1623	2009 Dec. 25	3192	LB1O24AFQ
G160M	1623	2009 Dec. 26	3192	LB1O23F2Q

^a Exposure identification code in the Mikulski Archive for Space Telescopes (see <http://archive.stsci.edu/index.html>).

et al. 2011). We will also show that these Ne VIII systems are remarkably metal-rich, and when information on nearby galaxies is available, the Ne VIII systems tend to be surprisingly far from luminous galaxies. The organization of the paper is as follows: In § 2, we discuss the COS observations and data handling, details of the analysis of each absorption system are given in § 3, § 4 describes the ionization modeling, results are given in § 5, a discussion of the galaxies in the field are given in § 6, and § 7 gives a summary and discussion. Throughout this paper we assume the 737 cosmology: $H_0 = 70 \text{ km s}^{-1} \text{ Mpc}^{-1}$, $\Omega_m = 0.3$, and $\Omega_\Lambda = 0.7$.

2. OBSERVATIONS

The observations of PG1148+549 presented here were taken as part of *HST* program 11741 (PI Tripp), a blind survey for highly ionized species such as O VI, Ne VIII, and Mg X, as well as lower ionization stages that constrain the physical conditions and metallicity of the multiphase galactic halos, in the spectra of $z \sim 1 - 1.5$ UV-bright quasars. Targets for this sample were selected only based on their redshift ($z \geq 0.9$) and flux in the far ultraviolet (FUV). No consideration was given to previously known information about absorption systems when selecting targets for this program, with two exceptions: (1) If a target was known to have a broad absorption line system in its spectrum, it was excluded because such systems, which are known to be ejected gas located very close to the QSO nucleus, have complex and temporally variable absorption profiles that spread over large wavelength ranges (see, e.g., Trump et al. 2006) and seriously compromise our ability to study *intervening* gaseous halos and intergalactic gas clouds. (2) If a target was known to have strong Lyman limit absorber that completely suppresses the flux shortward of its redshifted Lyman limit in some portion of the COS FUV band, the target was excluded in order to maximize the wavelength range that can be usefully searched for the species of interest.⁹

⁹ Note that a target was not rejected if its spectrum showed a *partial* Lyman limit, i.e., only a fully black Lyman limit absorption led to rejection.

While PG1148+549 had been previously observed with the *HST* Faint Object Spectrograph (FOS, $R \sim 1300$) in programs 4952 and 6210 (Hamann et al. 1998; Bechtold et al. 2002), the resolution and sensitivity of the FOS spectra are far too low for the purposes of this work, which requires detection of ≈ 20 mÅ lines and precise and reliable measurement of line centroids, line widths, and profile kinematics/component structure.

As summarized in Table 1, the COS spectra of PG1148+549 were acquired on 25-30 December 2009. To cover the full FUV wavelength range of COS from 1150 to 1800 Å, observations were obtained with both the G130M and G160M gratings, and for each grating two central wavelength tilts were used to fill in the gap between the two COS detector segments. In addition, several exposures with multiple focal-plane positions (FP-splits) were obtained with each central-wavelength setting so that the effects of fixed-pattern noise are mitigated when the individual exposures are aligned and combined. Overall, the total exposure times were estimated based on the goal of detecting Ne VIII lines as weak as those reported by Savage et al. (2005), i.e., exposure times were calculated to achieve adequate signal-to-noise (S/N) to detect lines with equivalent widths of 20 – 30 mÅ with good statistical significance over the full wavelength region where the doublet is redshifted into the *HST* bandpass.

The COS data were processed in the same manner as described in Meiring et al. (2011). The COS FUV detector backgrounds are very low (Green et al. 2012), so in the cores of strong absorption lines, the total counts can be low enough so that Poissonian statistics should be used to estimate the flux uncertainties. Since COS has photon-counting detectors, we used the counts in each pixel to determine flux uncertainties, using Poissonian statistics in regions of low counts. In addition to multiple FP-split exposures, flatfielding was applied to further reduce residual fixed-pattern noise, primarily from the COS gridwires. Strong and narrow absorption lines were used to cross correlate and align the individual exposures, and the reduced and coadded spectra were binned by 3 pixels since the standard pipeline COS data are oversampled with a ~ 6 pixel wide resolution element (i.e., the data were binned to Nyquist sampling of ~ 2 pixels per resolution element). All measurements and analyses in this paper were performed on the binned spectra. The binned spectra have a resolution of 15 – 20 km s⁻¹ per resolution element, and the signal-to-noise ratio of the final, fully combined COS spectrum ranges from 20 to 40 per resolution element, with S/N > 29 in most continuum pixels between 1180 and 1550 Å.

In principle, there are several potential sources of noise in addition to photon-counting statistics such as uncertainties in the continuum placement, uncertainties in the flux zero point, and fixed-pattern noise. Due to the low detector backgrounds of COS, uncertainties in the flux zero point are very small and can be safely neglected. We also expect the fixed-pattern noise contribution to be small due to our use of FP splits and flatfielding. To check this, we have measured the RMS noise in line-free continuum regions across the full wavelength range of the spectrum, and we find that the noise in the continuum is in good agreement with the expected noise based on photon-counting statistics, which indicates that fixed-

pattern noise makes a small and generally unimportant contribution to the overall measurement uncertainties. However, in some regions, continuum-placement uncertainty can be comparable to the statistical noise, so we have included this term in our error analyses.

While the COS FUV absorption lines are the central data of this survey, we also obtained several ancillary observations from the ground to support the COS analyses:

First, to search for Mg II $\lambda\lambda 2796, 2803$ absorption affiliated with systems of interest, we obtained high-resolution optical spectra of PG1148+549 with the High Resolution Echelle Spectrograph (HIRES) at the Keck Observatory. Two 900-second exposures were recorded with HIRESb on 2012 April 13 covering the 3300 – 5880 Å range with a spectral resolution of 6 km s⁻¹ (FWHM). In the wavelength range relevant to the absorption systems studied in this paper, the HIRES data have S/N = 40 to 50 per resolution element at the expected wavelengths of the Mg II doublet.

Second, we obtained deep multiband imaging of the PG1148+549 field with the twin Large Binocular Cameras (LBCs) on the 2×8.4-m Large Binocular Telescope (LBT). The LBCs, fully described in Giallongo et al. (2008), provide simultaneous imaging in two bands over a $\sim 23'$ field of view centered on the QSO. We obtained imaging in the UBVI bands, dithering between exposures to fill in the inter-chip gaps between the four CCDs. The total U and I band exposures total 2500 sec, while the B and V band exposures total 350 sec. The imaging was taken through very light cirrus with $\sim 1.0''$ seeing. In the current paper we make use of the LBC blue-side imaging; the U and B-band images reach 5σ limiting magnitudes of $U_{AB} \sim 26.0$ and $B_{AB} \sim 25.5$ mag in a $2''$ aperture. This is roughly equivalent to $L \sim 0.1 - 0.2 L^*$ at $z \sim 0.7$.

Finally, using the instrument setup and data-reduction procedures of Werk et al. (2012), we measured the redshifts, star-formation rates, and metallicities of galaxies close to the PG1148+549 sight line using the Keck Low Resolution Imaging Spectrometer (LRIS). Four of the brightest objects within $45''$ of the sight line were targeted with LRIS, with exposure times ranging from 600 to 800 s, on 2010 April 5. The LRIS spectra verified that two of the targets are stars, but the other two objects are galaxies, including a galaxy at the redshift of one the Ne VIII absorbers.

3. ABSORPTION-LINE MEASUREMENTS

After normalizing the continuum in regions of interest by interactively fitting cubic splines to the data, we employed two techniques for absorption-line measurements. First, we used the apparent column density method (Savage & Sembach 1991; Jenkins 1996) in which the apparent optical depth in a pixel, $\tau_a(v) = \ln[I_c(v)/I(v)]$, where $I(v)$ is the observed flux and $I_c(v)$ is the continuum flux at velocity v , is used to estimate the column density in that pixel, $N_a(v) = (m_e c / \pi e^2) \tau_a(v) / (f \lambda)$, where f is the oscillator strength and λ is the wavelength of the transition, and the other symbols have their usual meanings. Apparent column density profiles are useful in a variety of ways: (1) the profiles provide an efficient means to confirm line identifications, (2) $N_a(v)$ profiles can be scaled and overplotted to visually compare the kinematics and component structure of various species, and (3) the apparent column density profiles provide a

quick assessment of whether lines are affected by saturation (through comparison of weak vs. strong transition of a specific species). If a profile is not affected by saturation, it can be integrated to obtain the total column density, $N(\text{total}) = \int N_a(v)dv$.

Second, we used Voigt profile fitting to determine the column densities, velocity centroids, and b -values of H I and metal absorption lines detected in the PG1148+549 spectrum. To account for the broad wings in the COS line-spread function (Ghavamian et al. 2009; Green et al. 2012), the synthetic Voigt profiles were convolved with the COS line spread functions (LSF) at the nearest tabulated wavelength (Ghavamian et al. 2009). Whenever possible, multiple transitions were fit simultaneously (e.g. Lyman β, γ, δ) to determine the best fitting column densities.

This paper is focused on Ne VIII/O VI absorption systems, but since previous studies have always found that these systems also exhibit absorption from lower ionization stages, we have also searched for absorption lines from the strongest species expected in warm ionized gas as well. In the COS data, we search for ions of carbon, nitrogen, oxygen, and sulfur, and we use the Keck spectra to place upper limits on Mg II. Upper limits on column densities for non-detected species were derived by determining a 3σ upper limit on the rest-frame equivalent width of the undetected ion, including an allowance for continuum placement uncertainty using the method of Sembach & Savage (1992), and then the equivalent width upper limit was converted to a column density upper limit assuming the linear curve of growth applies. Often the COS data cover multiple transitions of a given ion; our strategy for placing upper limits is to use the strongest transition (and thereby obtain the tightest constraint) that is not badly affected by blending with unrelated lines.

The COS wavelength solution is known to have inaccuracies at the level of one to two (binned) pixels, and these inaccuracies are particularly noticeable in regions of the spectra that are recorded near the edges of the detector segments (Savage et al. 2011b); the worst errors can approach 30 km s^{-1} , although typically the errors are smaller than this. In some cases, we are able to correct for this wavelength calibration problem by comparing lines that should be well-aligned (e.g., H I Lyman series lines or different transitions of the same metal ion), and we have applied shifts in velocity to improve the wavelength calibration when such comparisons have been possible. We define the systemic redshifts of the absorbers to be the centroid of the strongest component of the O VI profiles.

4. NE VIII ABSORPTION SYSTEMS

Using the line-identification procedure of Tripp et al. (2008), we have identified three Ne VIII absorption systems in the spectrum of PG1148+549 at $z = 0.68381, 0.70152, 0.72478$. In addition to Ne VIII, we detect multiple ionization stages of oxygen, nitrogen, and carbon in these absorption systems, and we are able to place strong constraints on the H I content of the absorption systems, at least for the cooler phases. In this section we present basic information and measurements for these Ne VIII systems.

Table 2
Equivalent Widths and Integrated Apparent Column Densities for Transitions Observed in the $z_{\text{abs}}=0.68381$ System.

Transition	W_r (mÅ)	$\log [N_a \text{ (cm}^{-2}\text{)}]$
H I $\lambda 1025.72 \dots$	276 ± 17	14.77 ± 0.02
H I $\lambda 949.74 \dots$	54 ± 15	14.74 ± 0.11
H I $\lambda 937.80 \dots$	37 ± 9	14.82 ± 0.09
C II $\lambda 903.62^b \dots$	$< 19^c$	$< 13.2^d$
O II $\lambda 834.47 \dots$	$< 24^c$	$< 13.5^d$
Mg II $\lambda 2796.35$	$< 20^{c,e}$	$< 11.7^d$
N III $\lambda 685.51 \dots$	$< 34^c$	$< 13.5^d$
C III $\lambda 977.02 \dots$	188 ± 12	13.65 ± 0.02
S III $\lambda 698.73 \dots$	$< 15^c$	$< 12.7^d$
N IV $\lambda 765.15 \dots$	80 ± 8	13.47 ± 0.04
O IV $\lambda 787.71 \dots$	153 ± 8	14.60 ± 0.02
S IV $\lambda 809.67 \dots$	$< 15^c$	$< 13.4^d$
O VI $\lambda 1031.93 \dots$	234 ± 19	14.47 ± 0.03
O VI $\lambda 1037.62 \dots$	149 ± 23	14.50 ± 0.06
S VI $\lambda 944.52 \dots$	$< 35^c$	$< 13.3^d$
Ne VIII $\lambda 770.41$	51 ± 12	13.98 ± 0.09

^a The O III $\lambda 702.33$ and $\lambda 832.93$ lines are detected but are not listed in this table because both of these transitions are significantly blended with unrelated absorption features (see Figure 1), and thus the integrated quantities are not very useful. We estimate the O III column densities by jointly fitting Voigt profiles to both O III lines as well as the blended lines.

^b We use the C II $\lambda 903.62$ instead of the stronger C II $\lambda 903.96$ transition because the 903.96 \AA line is blended into the wing of a strong Ly α line at $z_{\text{abs}} = 0.2525$.

^c Three σ upper limit obtained by integration over $-75 < v < 100 \text{ km s}^{-1}$.

^d Upper limit based on the 3σ upper limit on W_r , assuming the line is in the linear regime of the curve of growth.

^e Derived from the Keck/HIRES data.

Table 3
Column Densities from Profile Fits to the COS Data for the $z_{\text{abs}}=0.68381$ System.

Ion	v_{rad} (km s^{-1})	$\log [N \text{ (cm}^{-2}\text{)}]$	b (km s^{-1})
H I . . .	0	14.65 ± 0.02	39.9 ± 2.4
	40	14.24 ± 0.05	20.0 ± 3.2
C III . .	0	13.57 ± 0.02	22.5 ± 1.7
	40	13.16 ± 0.07	8.5 ± 2.2
O III . .	0	14.02 ± 0.03	20.5^a
	40	13.64 ± 0.06	16.2^a
O IV . .	0	14.49 ± 0.03	20.5 ± 1.8
	40	14.28 ± 0.04	16.2 ± 2.0
O VI . .	0	14.41 ± 0.02	31.5 ± 1.9
	40	13.88 ± 0.06	31.0 ± 5.0
N IV . .	0	13.32 ± 0.05	23.9 ± 2.7
	40	12.96 ± 0.07	22.1 ± 5.3
Ne VIII	0	13.95 ± 0.04	32.0 ± 5.0
	40^b	–	–

^a Due to the blending in this line, the b values for the components were fixed to the values determined from the O IV $\lambda 787$ line. We report the column density uncertainties formally derived by the profile-fitting procedure, but we note that these lines may suffer from larger systematic uncertainties due to the significant blending with unrelated absorption.

^b The Ne VIII $\lambda 770.41$ line is weak, and while its velocity width and shape are consistent with those of the stronger metal lines, the Ne VIII $\lambda 770.41$ profile does not provide enough leverage, at the S/N provided by our COS spectrum, to enable a two-component fit (see Figure 1), so we have fitted the profile with a single line at $v = 0 \text{ km s}^{-1}$.

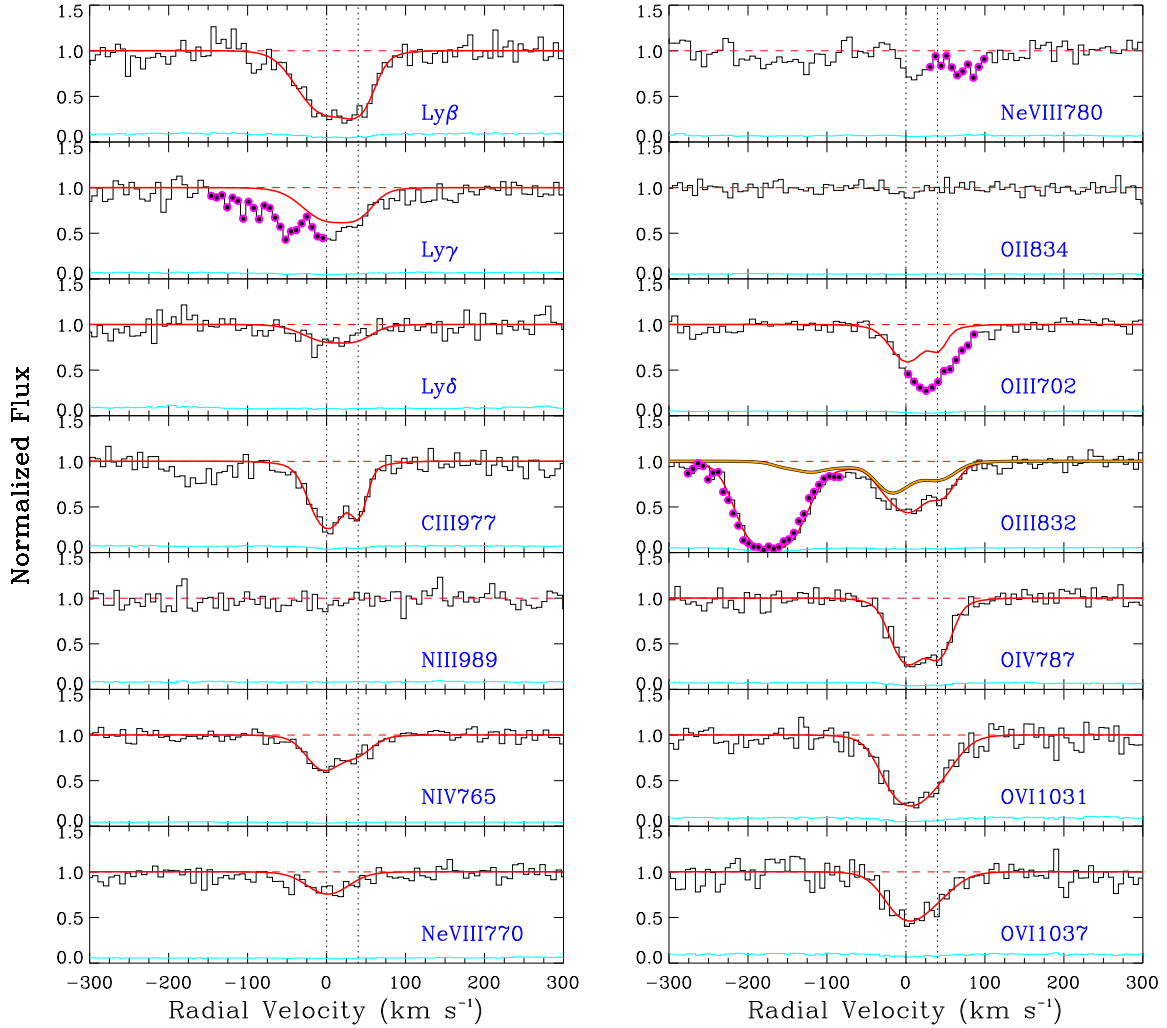


Figure 1. Continuum-normalized velocity plots of the absorption lines in the PG1148+549 Ne VIII absorber at $z_{\text{abs}}=0.68381$, plotted in the rest frame of the absorber (i.e., $v = 0 \text{ km s}^{-1}$ at $z_{\text{abs}}=0.68381$). Magenta points denote regions where the lines are blended with unaffiliated features from other systems, and the cyan line at the bottom of each panel denotes the 1σ error of the normalized flux. Vertical dotted lines mark the positions of the components, and the solid red line represents the best fit models determined from profile fitting. The O III λ 832 line is partially blended with the Si IV λ 1402 line from the Milky Way. The contribution from Si IV λ 1402 (based on the unblended Galactic Si IV λ 1393 profile) is shown with the solid orange line.

4.1. The $z_{\text{abs}}=0.68381$ system:

The Ne VIII absorber with the highest affiliated H I column density (and the largest number of affiliated metals) is the system at $z_{\text{abs}}=0.68381$. In this absorber we detect lines of H I, C III, O III, N IV, O IV, O VI, and Ne VIII. We also find a marginal feature at the expected wavelength of the strongest O II line at 834.47 Å; however, the significance of this feature is $< 3\sigma$, so we can only place an upper limit on $N(\text{O II})$. Likewise, no statistically significant N III lines are evident. Velocity plots for H I and metal-line absorption profiles for this system are shown in Figure 1; in this figure and in all velocity plots in this paper, the velocity scale is in the rest frame of the absorber, and we define the systemic redshifts of the absorbers to be the centroid of the strongest component of the O VI absorption profiles. Note that

in this figure (and the analogous figures for the other absorbers), we show some lines to alert the reader to problematic blends with lines from other redshifts, which are marked with magenta dots. In Figure 1, the best-fit Voigt profiles are overlaid in red. We have used two components to fit the absorption lines in this system. At this redshift, the H I Lyman α line is redshifted beyond the long-wavelength end of the COS spectrum. However, we detect H I transitions from Lyman β up to Lyman ϵ (λ 937.80) in the COS FUV spectrum (see Fig. 1). Rest-frame equivalent widths and integrated apparent column densities of the H I and metal lines in this system are given in Table 2, and column densities determined by Voigt profile fitting are listed in Table 3.

To support our line identifications, we compare the apparent column density profiles of the O IV λ 787.71, O VI λ 1031.93, 1037.62, and Ne VIII λ 770.41, 780.32 lines

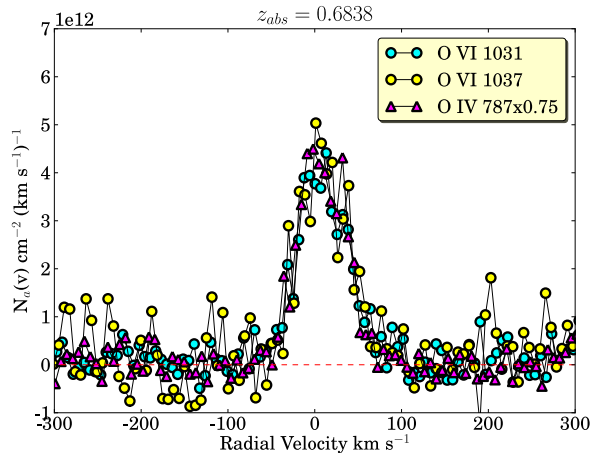


Figure 2. Apparent column density profiles (§ 3) of the O IV and O VI lines from the $z_{\text{abs}}=0.68381$ system. The O IV λ 787 line has been scaled by a factor of 0.75 for illustration. As in Figure 1 and all velocity plots in this paper, the velocity scale is in the rest frame of the absorption system. The y axis is plotted in units of 10^{12} particles cm^{-2} $(\text{km s}^{-1})^{-1}$.

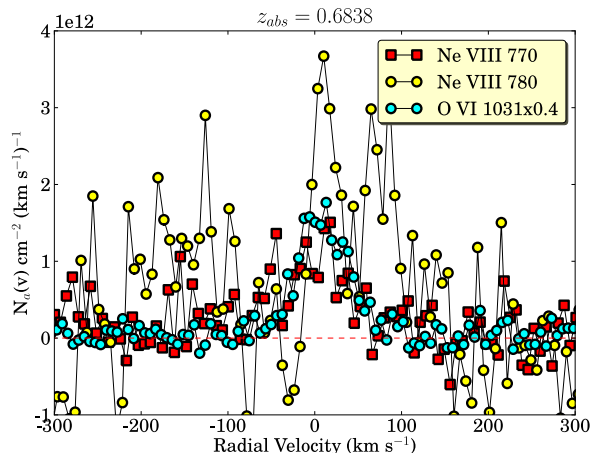


Figure 3. Apparent column density profiles of the O VI and Ne VIII lines from the $z_{\text{abs}}=0.68381$ system. The O VI λ 1031 line has been scaled by a factor of 0.4 for illustration.

in Figures 2 and 3. While there are multiple resonance transitions of O IV in the FUV (Verner et al. 1994), at $z_{\text{abs}}=0.68381$, only the O IV λ 787.71 line is redshifted into the wavelength range of our COS spectrum. Therefore, one might question the reliability of the O IV identification. However, as we can see from Figures 1 and 2, the profile of the O IV λ 787.71 line matches the profiles of the O VI doublet over a large span of pixels, and this indicates that the O IV identification is secure.

Similarly, the $N_a(v)$ plots are helpful for the Ne VIII identification. The Ne VIII λ 780.32 line is certainly blended with O III λ 832.93 at $z_{\text{abs}}=0.57757$, and this Ne VIII transition could also be blended with C III λ 977.02 at $z_{\text{abs}}\approx 0.3448$.¹⁰ The O III blend is securely identified; the $z_{\text{abs}}=0.57757$ absorber shows many H I

¹⁰ There are hundreds of absorption lines in the COS spectrum of PG1148+549, and a full summary of the lines in the spectrum is beyond the scope of this paper. We plan to analyze other systems in future papers.

Lyman series lines and metals with a distinctive two-component structure that matches the O III profile. One of the O III components at $z_{\text{abs}}=0.57757$ is redward of the expected wavelength of Ne VIII 780.32 line, but the other O III component falls near the center of the expected Ne VIII feature. The contribution of C III λ 977.02 at $z_{\text{abs}}\approx 0.3448$ to this blend is less certain; a well-detected Ly α line is found at $z_{\text{abs}}=0.3448$, and while this Ly α absorber has very few affiliated metals, C III λ 977.02 is one of the strongest FUV lines, and there could be some optical depth from C III in the blend as well. Given these blends, it is not surprising that the Ne VIII λ 780.32 profile appears to be stronger than the Ne VIII 770.41 line (see Figure 3) because some of the optical depth in the Ne VIII 780.32 profile is due to other species at other redshifts. Unfortunately, only one O III line from $z_{\text{abs}}=0.57757$ is redshifted into the COS spectrum, so we cannot remove the O III optical depth from the blend by modeling. Therefore, we must rely on the (unblended) Ne VIII λ 770.41 transition alone in the $z_{\text{abs}}=0.68381$ absorber. We can find no other plausible metal-line identifications for the Ne VIII λ 770.41 candidate, and the fact that the shape of the Ne VIII λ 770.41 profile matches the shape of the well-detected O VI lines at this redshift (see Figures 1 and 3) supports the identification of the feature as Ne VIII.

Finally, we note that the O III λ 832.93 line at $z_{\text{abs}}=0.68381$ is blended with the Milky Way Si IV λ 1402.77 transition. In this case, we can correct for the blend by modeling; by fitting the corresponding Milky Way Si IV λ 1393 line, we can predict the strength of the Si IV λ 1402.77 contamination (shown with an orange line in Figure 1) and account for it in our fitting of the O III λ 832.93 profile. A strong Lyman α line at $z_{\text{abs}}=0.1529$ is also observed near the O III λ 832.93 line (at -175 km s^{-1} ; see Figure 1). This Ly α line could contribute some optical depth to the O III feature as well due to the extended wings of the COS LSF, so this Ly α feature was also included in the multiline fit to the O III at $z_{\text{abs}}=0.68381$.

4.2. The $z_{\text{abs}}=0.70152$ system

A variety of absorption lines from metals are evident at $z_{\text{abs}}=0.70152$, including C III, O III, O IV, O VI, and Ne VIII. We do not detect N III or N IV, but the only N IV transition that is redshifted into the COS spectrum is lost in a blend with the strong Galactic O I λ 1302.17 absorption line. The N III λ 989.80 line is blended with a Lyman α line at $z_{\text{abs}}=0.3862$, but the N III 685.51 transition, which is nearly two times stronger, is not observed either. As in the $z_{\text{abs}}=0.68381$ system, the H I Ly α line is redshifted out of the COS spectrum, but unlike the $z_{\text{abs}}=0.68381$ absorber, no higher Lyman series lines are detected in the $z_{\text{abs}}=0.70152$ system. Velocity plots of the absorption lines from this system, including the undetected Ly β line, are shown in Figure 4, with the best fit profiles overlaid in red. Equivalent widths and column densities for the $z_{\text{abs}}=0.70152$ absorber, measured with the apparent column density technique and profile fitting, can be found in Tables 4 and 5. Two well-detected components at $v=0$ and 59 km s^{-1} are readily apparent in the absorption profiles of C III, O IV, and O VI, but Ne VIII is clearly detected only in the $v=0$ km s^{-1} feature. A third component is clearly seen at $v=-125$ km s^{-1}

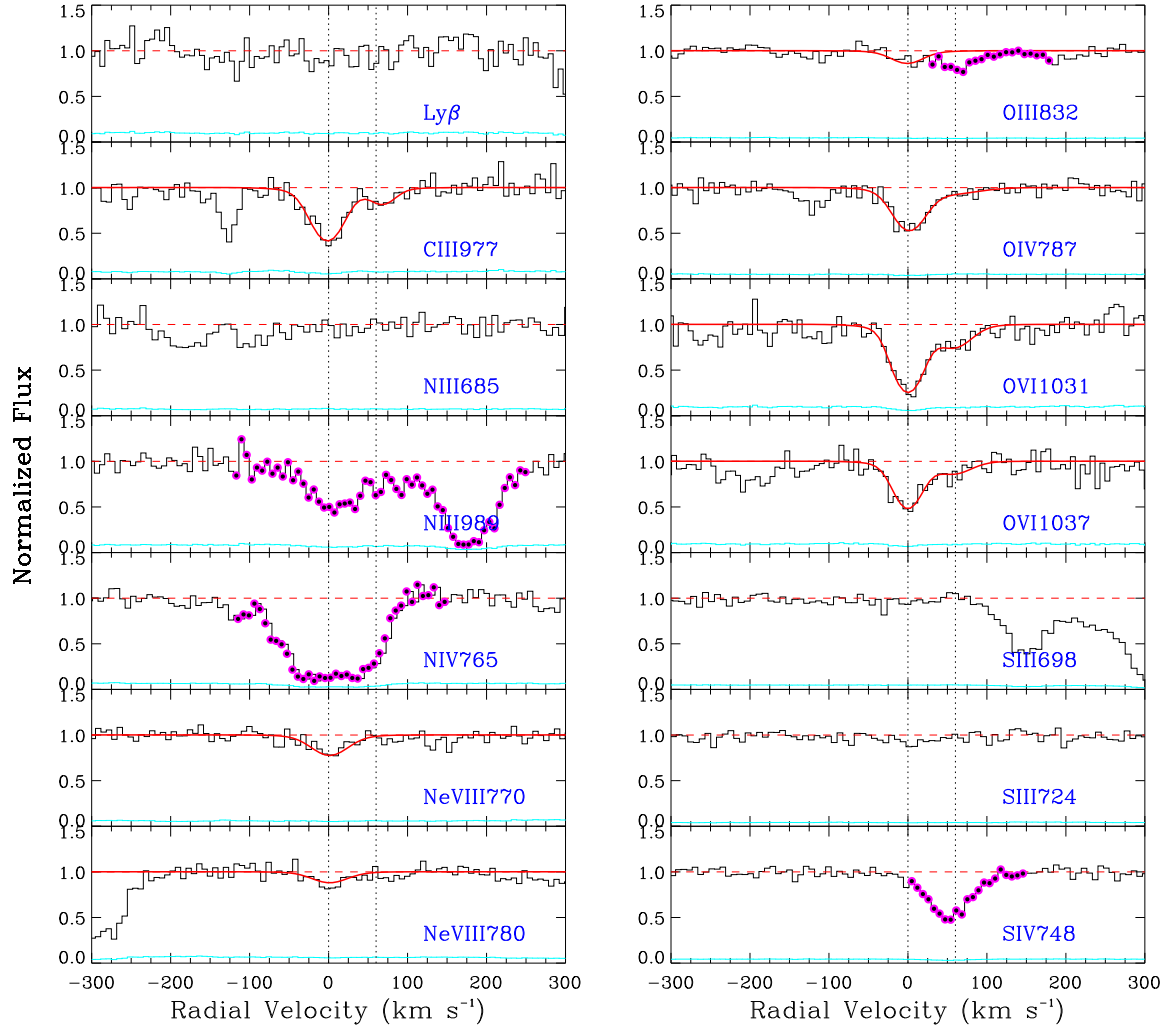


Figure 4. Continuum-normalized absorption profiles of the $z_{\text{abs}}=0.70152$ absorption system plotted in the rest frame of the absorber, as in Figure 1.

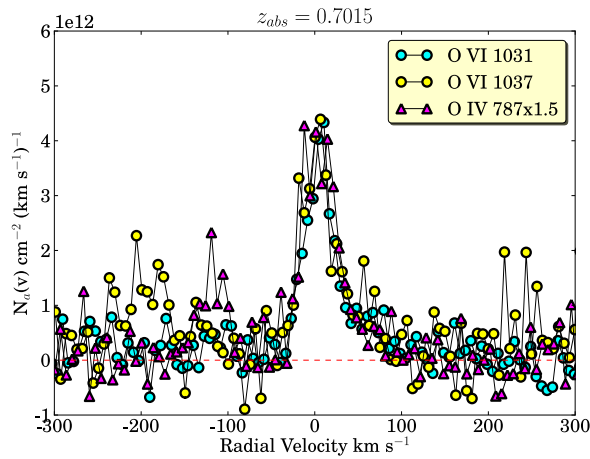


Figure 5. Apparent column density profiles of the O IV and O VI lines from the $z_{\text{abs}}=0.70152$ system. The O IV λ 787.71 line has been scaled by a factor of 1.5 for illustration.

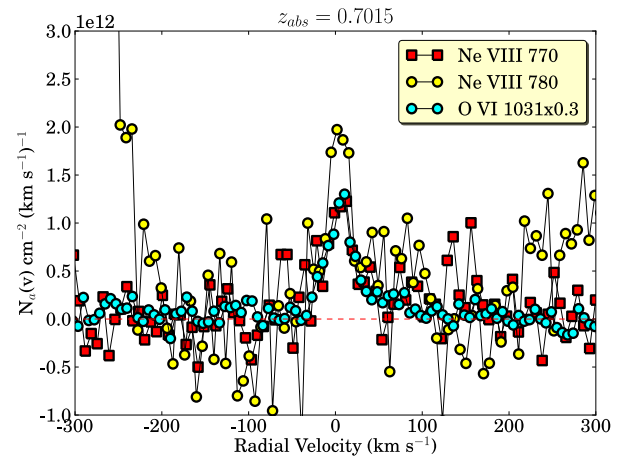


Figure 6. Apparent column density profiles of the O VI and Ne VIII lines from the $z_{\text{abs}}=0.70152$ system. The O VI λ 1031.93 line has been scaled by a factor of 0.3 for illustration.

Table 4
Equivalent Widths and Integrated Apparent Column Densities
for Transitions Observed in the $z_{\text{abs}}=0.70152$ System^a

Transition	W_r (mÅ)	$\log [N_a(\text{cm}^{-2})]$
H I $\lambda 1025.72 \dots$	$< 36^b$	$< 13.7^c$
C II $\lambda 903.96 \dots$	$< 18^b$	$< 12.9^c$
N II $\lambda 915.61 \dots$	$< 31^b$	$< 13.4^c$
O II $\lambda 834.47 \dots$	$< 20^b$	$< 13.4^c$
Mg II $\lambda 2796.35$	$< 17^{b,d}$	$< 11.6^c$
C III $\lambda 977.02 \dots$	126 ± 16	13.41 ± 0.05
N III $\lambda 685.51 \dots$	$< 26^b$	$< 13.4^c$
O III $\lambda 832.93 \dots$	18 ± 5	13.48 ± 0.09
S III $\lambda 698.73 \dots$	$< 13^b$	$< 12.6^c$
O IV $\lambda 787.71 \dots$	75 ± 9	14.18 ± 0.04
S IV $\lambda 809.67 \dots$	$< 19^b$	$< 13.5^c$
S V $\lambda 786.48 \dots$	$< 20^b$	$< 12.4^c$
O VI $\lambda 1031.93 \dots$	168 ± 19	14.29 ± 0.04
O VI $\lambda 1037.62 \dots$	113 ± 19	14.35 ± 0.06
S VI $\lambda 933.38 \dots$	$< 30^b$	$< 12.9^c$
Ne VIII $\lambda 770.41$	28 ± 5	13.75 ± 0.07
Ne VIII $\lambda 780.32$	18 ± 6	13.86 ± 0.11

^a Quantities in this table do not include the weak component at $v = -125 \text{ km s}^{-1}$, which is only marginally detected in O VI and is not detected in Ne VIII.

^b Three σ upper limit obtained by integration over $-50 < v < 100 \text{ km s}^{-1}$.

^c Upper limit based on the 3σ upper limit on W_r , assuming the line is in the linear regime of the curve of growth.

^d Derived from the Keck/HIRES data.

s^{-1} in the C III and O IV transitions, and weak but consistent features are present at this velocity in O III and O VI. The O VI at this velocity is particularly marginal; the feature is only seen in the $\lambda 1031.93$ line and is not confirmed by the (albeit noisy) $\lambda 1037.62$ profile. In this paper, we focus on the two components at $v = 0$ and 59 km s^{-1} that are well-detected in O VI. Higher S/N would be helpful for the study of weaker features such as the $v = -125 \text{ km s}^{-1}$ component.

As in the previous section, we also compare the N_a profiles of O IV, O VI, and Ne VIII in Figures 5 and 6 to aid our comments about line identification. We can see from Figure 5 that the O IV $\lambda 787.71$ identification is unambiguous; the O IV and O VI profiles match precisely, including an asymmetric wing extending to positive velocities. We can see that this wing is due to a weak component at $v = +60 \text{ km s}^{-1}$, and we fit the profiles with two components at $v = 0$ and $+60 \text{ km s}^{-1}$. The Ne VIII $\lambda 780.32$ profile shows some excess optical depth compared to the Ne VIII $\lambda 770.41$ line (Figure 6). This could be due to noise, but we note that there appears to be some additional excess absorption on the red side of the 780.32 \AA line, and it possible that the Ne VIII $\lambda 780.32$ profile is weakly contaminated by an interloper, likely a weak Ly α line from lower redshift. However, the good match of the Ne VIII $\lambda 770.41$ profile to the O IV and O VI profiles indicates that reliable Ne VIII measurements can be obtained from the 770.41 \AA data.

The absence of Ly β absorption is an interesting feature of this absorber – combined with detection of strong metal lines, this suggests that this is a highly metal enriched system, as we will discuss further in §5. Integrating over the full velocity range of the detected metal absorption ($-50 < v < 100 \text{ km s}^{-1}$), we obtain $\log N(\text{H I})$

Table 5
Column Densities from Profile Fits to the COS Data for the
 $z_{\text{abs}}=0.70152$ System

Ion	v_{rad} (km s^{-1})	$\log [N(\text{cm}^{-2})]$	b (km s^{-1})
C III ..	-125	13.24 ± 0.24	6.3 ± 3.2
	0	13.39 ± 0.03	23.9 ± 2.2
	59	12.63 ± 0.10	18.7 ± 6.9
O III ..	-125	13.39 ± 0.07	20.4 ± 7.7
	0	13.55 ± 0.06	23.9 ± 5.5
	59	–	–
O IV ..	-125	13.63 ± 0.06	14.8 ± 4.6
	0	14.17 ± 0.02	23.7 ± 1.9
	59 ^a	13.33 ± 0.15^a	42.7 ± 21.0^a
O VI ..	-125 ^b	13.46 ± 0.14^b	32.4 ± 19.1^b
	0	14.28 ± 0.03	20.9 ± 2.0
	59	13.63 ± 0.12	27.3 ± 10.3
Ne VIII	-125	–	–
	0	13.82 ± 0.06^c	28.2 ± 7.1^c
	59	–	–

^a While O IV absorption is clearly present at this velocity, the parameters of this component are more uncertain due to the intrinsic weakness of the component and its significant blending with the stronger adjacent component at $v = 0 \text{ km s}^{-1}$.

^b This component is marginally detected in the stronger $\lambda 1031.93$ transition and is not adequately detected in the weaker $\lambda 1037.62$ line; consequently, the parameters of the component are highly uncertain.

^c The Ne VIII $\lambda 780.32$ line is affected by a blend (see text), so the results in this table are based on a fit to the Ne VIII $\lambda 770.41$ transition only.

< 13.7 (3σ). However, we noted above that two components are evident in this system, and will consider the implied metallicities of this absorber on a component-by-component basis in the following section, so have also obtained limits on $N(\text{H I})$ in each of the components. For the feature at $v = 0 \text{ km s}^{-1}$, we integrate from -50 to 50 km s^{-1} and obtain $\log N(\text{H I}) < 13.6$ (3σ). For the $v = 60 \text{ km s}^{-1}$ component, we integrate from 50 to 100 km s^{-1} and obtain $\log N(\text{H I}) < 13.4$ (3σ).

4.3. The $z_{\text{abs}}=0.72478$ system

The final Ne VIII absorber is similar to the system at $z_{\text{abs}}=0.70152$ with detections of O IV, O VI, and Ne VIII and no affiliated H I absorption in Ly β or higher Lyman series lines. We show a velocity stack plot of selected lines in Figure 7, and we compare the $N_a(v)$ profiles of O IV, O VI, and Ne VIII in Figures 8 and 9. The data indicate only a single component in this absorber. No H I absorption is detected, and we derive an upper limit of $\log N(\text{H I}) < 13.7$ by integrating the Lyman β $\lambda 1025$ line region from -75 to $+75 \text{ km s}^{-1}$. Equivalent widths and column densities for this system are summarized in Tables 6 and 7. The O IV $\lambda 787.71$ and O VI $\lambda \lambda 1031.93, 1037.62$ lines are detected in this system at high significance, and the good correspondence of the Ne VIII profiles with the other lines supports the Ne VIII identification.

5. IONIZATION MODELING

We now turn to analysis of the physical conditions and metallicity of the Ne VIII/O VI absorbers. Given the velocity alignment of the Ne VIII and O VI absorption lines

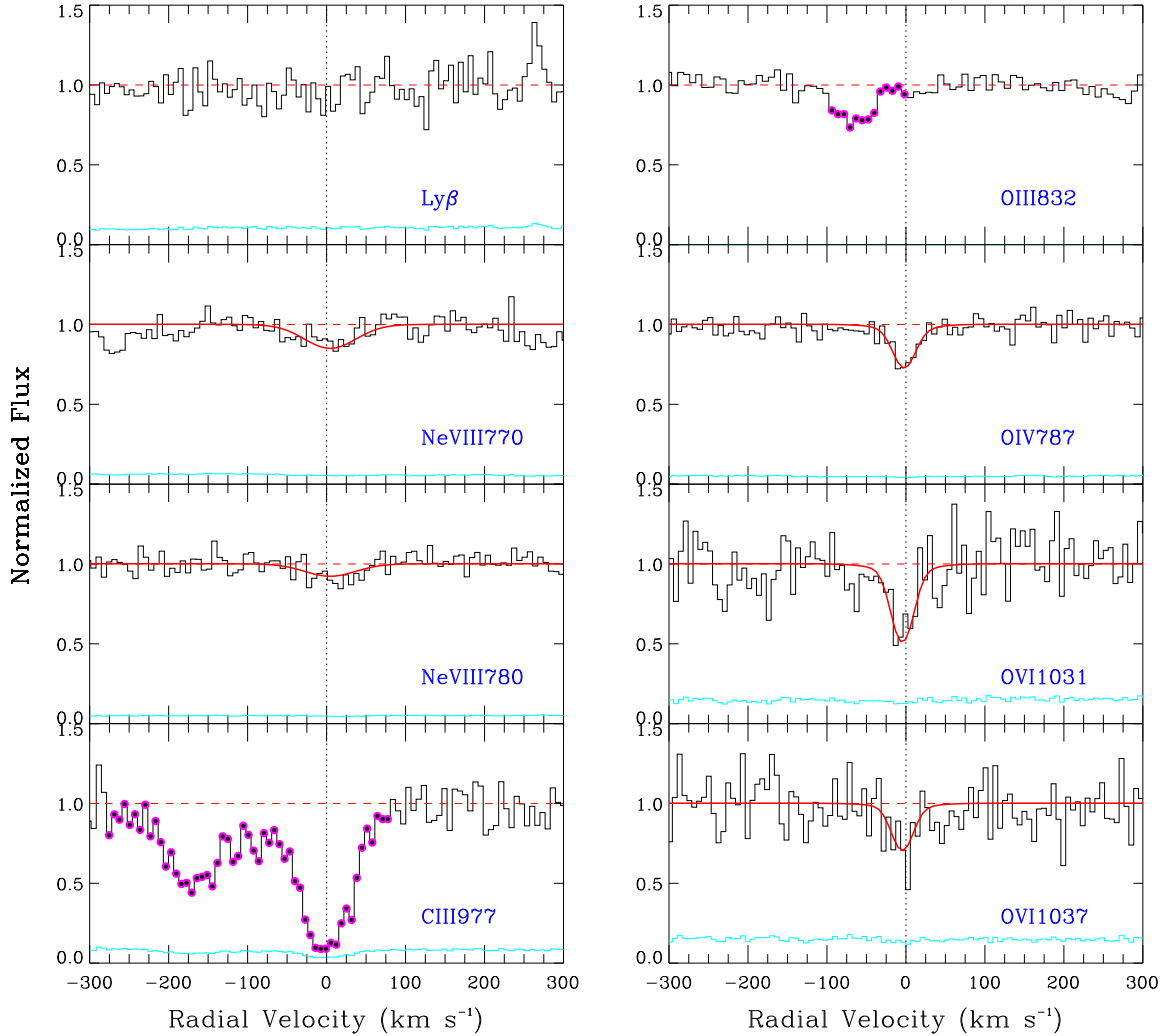


Figure 7. Continuum-normalized absorption profiles of the $z_{\text{abs}}=0.72478$ absorption system plotted in the rest frame of the absorber, as in Figure 1.

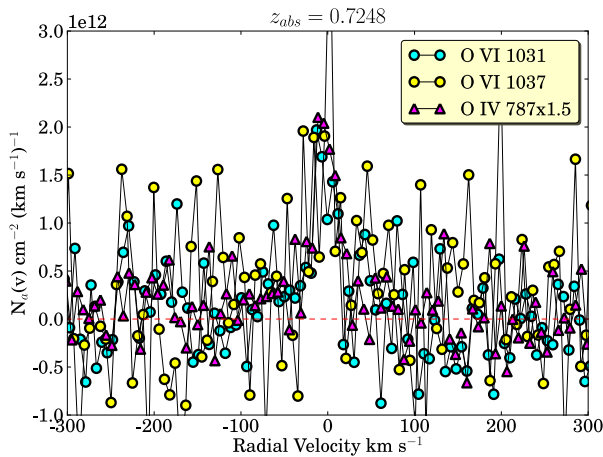


Figure 8. Apparent column density profiles of the O IV and O VI lines of the $z_{\text{abs}}=0.72478$ system. The O IV λ 787.71 line has been scaled by a factor of 1.5 for purposes of comparison.

with lower ionization stages, it is clear that there is some sort of relationship between the Ne VIII-bearing gas and the lower ionization material. The velocity alignment does not necessarily indicate that the Ne VIII arises in a single-phase cloud that is cospatial with the lower ions; it is possible that this indicates that the Ne VIII originates in an interface on the surface of a lower ionization cloud, for example. To investigate this relationship and probe the nature of the Ne VIII absorbers, we holistically analyze the ionization mechanism(s) for *all* detected ionization stages, not just the Ne VIII. For this purpose, we follow the methodology of Tripp et al. (2011), which is briefly summarized as follows. We first constrain the portion of the absorbing gas that can be attributed to low-density, cool gas that is photoionized by the UV background light (§ 5.1). Photoionization models of optically thin gas homologously depend on the ionization parameter U , which is the ratio of the number density of ionizing photons to the particle density ($U = n_\gamma/n_H$), the absolute and relative abundances of the elements, and

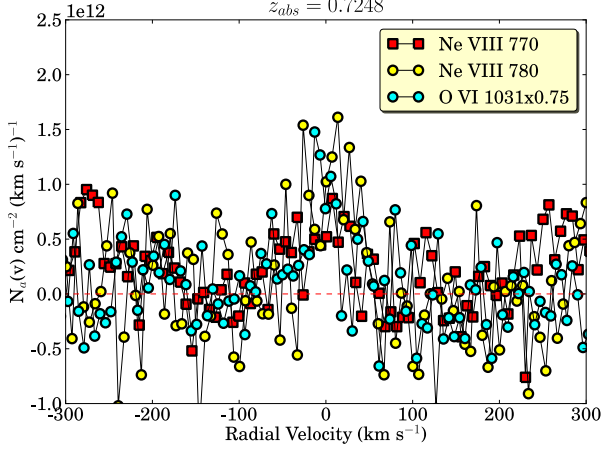


Figure 9. Apparent column density profiles of the O VI and Ne VIII lines from the $z_{\text{abs}}=0.72478$ system. The O VI λ 1031.93 line has been scaled by a factor of 0.75 for comparison with the other lines.

Table 6

Equivalent Widths and Integrated Apparent Column Densities for Transitions Observed in the $z_{\text{abs}}=0.72478$ System.

Transition	W_r (mÅ)	$\log [N_a \text{ (cm}^{-2}\text{)}]$
H I λ 1025.72...	< 30 ^a	< 13.7 ^b
C II λ 687.05...	< 13 ^a	< 12.9 ^b
N II λ 671.41...	< 23 ^a	< 13.9 ^b
O II λ 834.47...	< 15 ^a	< 13.5 ^b
Mg II λ 2796.35	< 16 ^{a,c}	< 11.6 ^b
N III λ 685.00 ^d	< 14 ^a	< 13.4 ^b
O III λ 832.93...	< 16 ^a	< 13.5 ^b
S III λ 677.75...	< 21 ^a	< 12.5 ^b
N IV λ 765.15...	< 26 ^a	< 12.9 ^b
O IV λ 787.71...	27 \pm 5	13.70 \pm 0.06
S IV λ 748.40...	< 13 ^a	< 12.7 ^b
S V λ 786.48...	< 14 ^a	< 12.2 ^b
O VI λ 1031.93.	71 \pm 20	13.84 \pm 0.10
O VI λ 1037.62.	37 \pm 12	13.87 \pm 0.15
S VI λ 933.38...	< 30 ^a	< 12.9 ^b
Ne VIII λ 770.41	26 \pm 8	13.70 \pm 0.12
Ne VIII λ 780.32	19 \pm 5	13.87 \pm 0.10

^a Three σ upper limit obtained by integration over $-75 < v < 75$ km s⁻¹.

^b Upper limit based on the 3σ upper limit on W_r , assuming the line is in the linear regime of the curve of growth.

^c Derived from the Keck/HIRES data.

^d We use the N III λ 685.0 transition to place this limit because the other N III lines in the COS spectrum at this redshift are confused by blending.

Table 7

Column Densities from Profile Fits to the COS Data for the $z_{\text{abs}}=0.72478$ System.

Ion	v_{rad} (km s ⁻¹)	$\log [N \text{ (cm}^{-2}\text{)}]$	b (km s ⁻¹)
O IV...	0	13.75 \pm 0.04	16.1 \pm 2.9
O VI...	0	13.86 \pm 0.07	15.8 \pm 3.8
NeVIII.	0	13.81 \pm 0.06	41.4 \pm 7.5

the hydrogen column density. In order to avoid modeling ambiguities resulting from degeneracies between ionization corrections and relative abundances, we use the O IV/O III column-density ratio to determine U , and we constrain the models to match the measurements of (or upper limits on) $N(\text{H I})$. With the ionization parameter constrained by O IV/O III, we then consider the column densities predicted by the photoionization models for the other species. We will find that the photoionization models predict O VI and Ne VIII column densities that are orders of magnitude lower than the observed $N(\text{O VI})$ and $N(\text{Ne VIII})$ values. Consequently, we then examine whether the O VI and Ne VIII can be attributed to a collisionally ionized hot phase (§ 5.2).

5.1. Photoionization

We model photoionized gas using CLOUDY version 8.00 (Ferland et al. 1998). We have used the Haardt & Madau extragalactic background spectrum (Haardt & Madau 1996) at $z = 0.7$, with the modifications and updates described in Haardt & Madau (2001), including contributions from both active galactic nuclei (AGN) and galaxies. We treat the absorbers as plane-parallel slabs with constant density, and we initially assume that the elements have the same relative abundances observed in the Sun (Lodders 2003; Asplund et al. 2009); after running the initial models, we consider whether there is evidence for departures from the solar abundance patterns. Local flux sources (starlight from galaxies) can be brighter than the diffuse UV background if the escape fraction of the ionizing flux is sufficiently high (Fox et al. 2005; Misawa et al. 2009). However, observational studies have not yet provided strong evidence of a high escape fraction, so we will mainly employ the Haardt & Madau (1996) flux as our fiducial model in this paper.

5.1.1. $z_{\text{abs}} = 0.68381$

Figure 10 shows our photoionization model for the component at $v = 0$ km s⁻¹ of the absorption system at $z_{\text{abs}} = 0.68381$. In this figure, the column densities predicted by the CLOUDY model are plotted with smooth curves, and the observed column densities and upper limits are displayed with large, discrete symbols at the value of U that matches the observed O IV/O III ratio (in some cases, small offsets have been applied for clarity because the symbols overlap). The legends in each panel label the curves and symbols. This model matches the observed O IV/O III ratio with $\log U = -1.60$ and metallicity¹¹ $[X/H] = -0.5$. Various parameters of this photoionization model are summarized in Table 8.

With the ionization parameter constrained by O IV/O III, several interesting implications unfold. First and foremost, this photoionization model falls woefully short of the observed column densities of O VI and Ne VIII: the observed $N(\text{O VI})$ is 25 times higher than the model prediction, and the observed $N(\text{Ne VIII})$ is many orders of magnitude higher than the model, which predicts negligible amounts of Ne VIII in the photoionized gas at $\log U = -1.6$. The high-ion absorption must arise in a separate phase. Second, the

¹¹ We use the usual notation where Z is the absolute metallicity and the logarithmic metallicity $[X/H] = \log [N(X)/N(\text{H})] - \log (X/H)_{\odot}$.

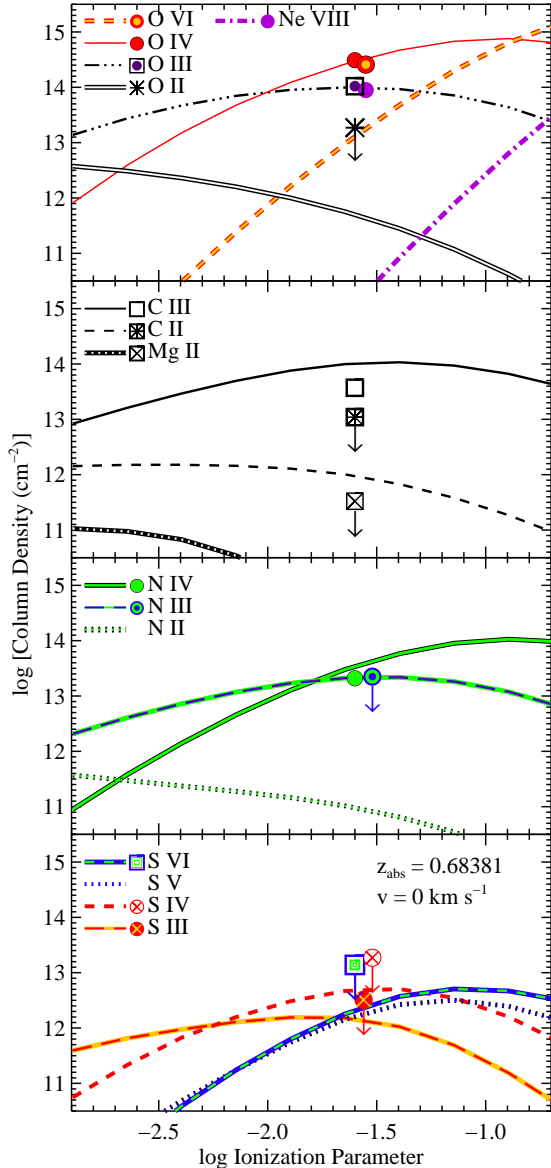


Figure 10. Photoionization modeling of the $v = 0 \text{ km s}^{-1}$ component in the multiphase O VI/Ne VIII absorber at $z_{\text{abs}} = 0.68381$, assuming the gas is photoionized by the diffuse UV background from quasars and galaxies as calculated by Haardt & Madau (2001). In each panel, the column densities predicted by the photoionization model, as a function of ionization parameter U , are shown with smooth curves. The observed column densities and 3σ upper limits are indicated with large symbols at $\log U \approx -1.6$. Generally, the uncertainties in the observed column densities are comparable to the symbol sizes (see Tables 2 – 7). The species corresponding to each curve and symbol are indicated by the legend in the upper-left corner of each panel. In this figure, the overall metallicity is $Z = 0.3Z_{\odot}$.

model is roughly consistent with the measurements for intermediate-ionization stages of carbon, nitrogen, and sulfur (lower panels). However, the model seems to require modest underabundances of carbon and nitrogen; the observed columns of both C III and N IV are somewhat lower than predicted by the model, and the upper limit on N III is also in tension with the model, which in-

dicates that N III should be marginally detected.¹² To fit the C III and N IV, this model requires modest relative abundance adjustments; relative to oxygen, the model requires $[\text{C}/\text{O}] = -0.4$ and $[\text{N}/\text{O}] = -0.2$. The upper limits on the sulfur ions are consistent with the model but do not provide additional information. The sulfur ion column densities are all expected to be below the detection threshold (lowest panel in Figure 10). However, the predicted sulfur columns are only moderately below the observed upper limits, so higher signal-to-noise observations could provide information on the relative abundances of sulfur as well. Even though the Mg II $\lambda\lambda$ 2796.35, 2803.53 doublet is extremely strong and places tight upper limits on $N(\text{Mg II})$, we see from Figure 10 that Mg II is easily photoionized in these conditions and is expected to be undetectable. Indeed, the photoionization model indicates that all of the low ions that we can constrain (e.g., C II, N II, O II, Mg II) should have very low column densities that are well below the observed upper limits. As we discuss below, underabundances of C and N are not necessarily surprising.

We note that the discrepancies between the model and the observed O VI and Ne VIII columns, as well as the underabundances implied by C III and N IV, cannot be attributed to measurement uncertainties; the column density uncertainties are generally smaller than the symbol sizes in Figure 10. A potential source of systematic uncertainty in this analysis is the assumed ionizing flux field. The shape and intensity of the UV background are constrained by models (e.g., Haardt & Madau 1996) but are only loosely constrained by observations (Davé & Tripp 2001, and references therein). In principle, with fine tuning, modifications of the shape of the radiation field could alleviate the C III and N IV discrepancies, but usually this is not helpful because the ionization potentials of O III/O IV, C III/C IV, and N III/N IV are too similar. The observations may be indicating real underabundances of C and N.

On the other hand, it is interesting to consider whether adjustments of the ionizing flux field could lead to higher O VI and Ne VIII columns and thereby alleviate this problem. For example, it is known that obscured AGN comprise an important portion of the X-ray background (e.g., Mushotsky et al. 2000; Gilli et al. 2007); could an obscured AGN near the PG1148+549 sight line change the ionizing flux field in a way that boosts the O VI and Ne VIII column densities? To explore this idea, we have used CLOUDY to produce models of an obscured AGN with obscuring columns as high as $\log N(\text{H}) = 23$. Our absorbers are optically thin and thus are always exposed to the UV background, so we combined the flux from the obscured AGN with the Haardt & Madau UV background with various mixtures of relative brightness of the two components of the model. Every variation of this obscured AGN + UV background model failed badly. As can be seen in, e.g., Figure 1d of Hamann (1997), obscuration of an AGN actually reduces the flux of photons capable of photoionizing Ne VII to produce Ne VIII more than it reduces the flux that can ionize O II, O III, O IV, etc., so adding an obscured AGN does

¹² We note that a weak feature is apparent at the expected wavelength of N III $\lambda 685.51$, but the feature is not recorded at adequate significance to provide a reliable measurement.

Table 8
Photoionization Model Parameters^a

Redshift	Component Velocity (km s ⁻¹)	log N(H I)	log N(H _{tot})	log U ^b	[X/H] ^c	[C/O] ^d	[N/O] ^d	Number Density (cm ⁻³)	Absorber Thickness (kpc)
0.68381...	0	14.65	18.49	-1.60	-0.5	-0.4	-0.2	2.9×10 ⁻⁴	3.5
0.68381...	40	14.24	18.24	-1.45	-0.5	-0.5	-0.4	2.0×10 ⁻⁴	2.8
0.70152...	0	<13.60	<17.54	-1.38	> 0.2	-0.1	-	1.8×10 ⁻⁴	<0.6
0.70152...	59 (Model 1) ^e	<13.40	<17.11	-1.67	> -0.2	-0.3	-	3.5×10 ⁻⁴	<0.1
0.70152...	59 (Model 2) ^e	<13.40	<18.31	-0.70	> -0.8	+0.5	-	3.7×10 ⁻⁵	<18
0.72478...	0 (Model 1) ^e	<13.70	<17.26	-1.75	> 0.0	-	-	4.4×10 ⁻⁴	<0.1
0.72478...	0 (Model 2) ^e	<13.70	<18.60	-0.70	> -0.7	-	-	3.9×10 ⁻⁵	<33

^a Photoionization modeling results, assuming the gas is photoionized by the UV background flux from QSOs and galaxies, as calculated by Haardt & Madau (1996) with the updates of Haardt & Madau (2001). Plausible modification of the ionizing flux field can systematically change photoionization model results by factors of ~ 2 (Aracil et al. 2006; Tripp et al. 2006; Stocke et al. 2013).

^b U = ionization parameter.

^c Logarithmic absolute abundance with respect to solar abundances, based on oxygen.

^d Logarithmic relative abundance of carbon and nitrogen with respect to their solar abundances compared to oxygen.

^e For components in which O III absorption is not detected, we consider two models. In model 1, the lower limit on the O IV/O III column-density ratio is used to find the minimum ionization parameter that is consistent with the O III and O IV constraints. In model 2, the measured column densities of O IV and O VI (which are both detected) are used to find the maximum ionization parameter allowed by the measurements. As discussed in the text, model 1 is strongly favored over model 2 in these cases, and at any rate, none of the photoionization models produce enough Ne VIII to match the observations in any of these three absorption systems.

not boost the Ne VIII or O VI column densities relative to the lower ionization stages.

It appears that the Ne VIII and O VI must arise in a separate gas phase from the lower ionization stages. But is the Ne VIII-bearing gas photoionized or collisionally ionized? We can rule out photoionized Ne VIII and O VI – our CLOUDY models indicate that in order to arise in photoionized gas, the observed Ne VIII and O VI columns would require very high values for U . With the Haardt & Madau flux at $z = 0.68$, this in turn requires very low densities and cloud sizes > 1 Mpc. Such large sizes would result in broadening of the lines by the Hubble flow that is not allowed by the measured line widths. Similar arguments have been made for other systems with Ne VIII detections, where the implied cloud sizes in the photoionized Ne VIII models leads to unrealistically large cloud sizes (Savage et al. 2005; Narayanan et al. 2011; Tripp et al. 2011; Narayanan et al. 2012).

As single-phase and two-phase photoionization models fail to account for both the low and high ions simultaneously, we conclude that the lower ions (O III, C III, O IV, etc.) reside in a photoionized core, and that the high ions (O VI and Ne VIII) reside in a collisionally ionized, hot phase. Such necessity of a collisionally ionized phase has also been demonstrated for other Ne VIII absorbers (Narayanan et al. 2009, 2011, 2012; Savage et al. 2005; Tripp et al. 2011). We will investigate the implied properties of the hot phase in § 5.2.

We have applied the same photoionization models to the component at $v = 40$ km s⁻¹ in the $z_{\text{abs}} = 0.68381$ absorption system. As summarized in Table 8, we obtain very similar results as we found for the $v = 0$ km s⁻¹ component, including the same overall metallicity ($Z = 0.3Z_{\odot}$), similar underabundances of carbon and nitrogen (relative to oxygen), and a similar ionization parameter.

5.1.2. $z_{\text{abs}} = 0.70152$ and 0.72478

We have used our CLOUDY photoionization models to similarly constrain the properties of the systems at $z_{\text{abs}} = 0.70152$ and 0.72478 , and our results are listed in Table 8. For these absorption systems, we only have upper limits

on the H I column density and we detect a more limited suite of metals, but we can, nevertheless, show that the physical conditions and metallicity are similar to those of the $z_{\text{abs}} = 0.68381$ system.

For the $v = 0$ km s⁻¹ component of the $z_{\text{abs}} = 0.70152$ absorber, the observed O IV/O III ratio indicates that $\log U = -1.38$ and, interestingly, the observed columns require a supersolar metallicity, $[X/H] > +0.2$. We can only place a lower limit on the metallicity since we only have an upper limit on $N(\text{H I})$; a decrease in the $N(\text{H I})$ assumed for the photoionization model [$\log N(\text{H I}) \leq 13.60$] would require an increase in the metallicity. However, in this component the evidence for a carbon underabundance is less compelling with $[C/O] = -0.1$, and we have no information about nitrogen. On the other hand, we once again draw a robust conclusion about the highly ionized gas: the O VI and Ne VIII column densities are orders of magnitude higher than expected in photoionization models – these models cannot simultaneously match O III, O IV, O VI, and Ne VIII in a single-phase gas cloud.

Due to blending, we are unable to measure $N(\text{O III})$ in the $v = 59$ km s⁻¹ component of the $z_{\text{abs}} = 0.70152$ system (see Figure 4), which leads to greater ambiguity in the modeling. We bracket the physical conditions and metallicity in this component by considering two photoionization models that are at the extreme ends of the ionization parameter range allowed by the data. These models are referred to as Model 1 and Model 2 in Table 8. In Model 1, we find the ionization parameter that matches the observed minimum O IV/O III ratio [based on the measured $N(\text{O IV})$ and the upper limit on $N(\text{O III})$]. As in the previous section, this model falls far short of the observed $N(\text{O VI})$. In Model 2, we find the value of U that matches the observed O IV/O VI ratio. By definition, Model 2 agrees with the measured $N(\text{O VI})$, but we note that this model does not produce enough Ne VIII compared to the observations.

While it only provides a lower limit on U , we argue that Model 1 is likely closer to the actual physical conditions

and metallicity of the gas for the following reasons. First, Model 2 does not predict enough C III compared to the measured $N(\text{C III})$, and in order to fit the data, we must invoke a substantial carbon overabundance. There is astrophysical precedence for a carbon *under*abundance – carbon underabundances are observed in stars in the disk and halo of the Milky Way (Akerman et al. 2004; Bensby & Feltzing 2006; Fabbian et al. 2009) as well as damped Ly α absorbers (Pettini et al. 2008; Penprase et al. 2010; Cooke et al. 2011). On the other hand, the combination of low metallicity and a high carbon overabundance required by Model 2, $[\text{X}/\text{H}] = -0.8$ and $[\text{C}/\text{O}] = +0.5$, is a rather peculiar abundance pattern. There are some “carbon-enhanced” damped Ly α systems (Cooke et al. 2012), but these absorbers have much lower metallicities than Model 2. It seems likely that Model 2 requires a carbon overabundance because the model is wrong. Second, as shown in Table 8, Model 1 implies absorber properties (e.g., density and size) that are similar to the characteristics of the other components where O III is detected, whereas Model 2 requires much lower densities and much larger gas clouds. Third, if we generally place the O VI in the same (cospatial) gas as the O IV, then it becomes hard to explain where the Ne VIII arises (Ne VIII must then originate in a phase that makes no contribution to the O VI column density). If we place the O VI in the Ne VIII-bearing gas, which is distinct from the O IV phase, then the Ne VIII is naturally explained, as we discuss below. At any rate, Models 1 and 2 bracket the allowed range of physical conditions, as summarized in Table 8.

The Ne VIII absorber at $z_{\text{abs}} = 0.72478$ is very similar to the absorption system at $z_{\text{abs}} = 0.70152$, and we have modeled the $z_{\text{abs}} = 0.72478$ system in the same way as we treated the absorber at $z_{\text{abs}} = 0.70152$. Our results for the $z_{\text{abs}} = 0.72478$ case are summarized in Table 8. As in the other systems studied in this paper, the $z_{\text{abs}} = 0.72478$ requires a high metallicity, as one might expect given the detection of metals and the absence of H I (Figure 7), and the presence of Ne VIII requires a hot, collisionally ionized phase.

5.2. Collisional Ionization

The photoionization models fail to produce enough O VI and Ne VIII to match the observed column densities because the required gas densities are too low and the cloud sizes are too large. Consequently, we now consider whether addition of a hot, collisionally ionized phase provides a viable explanation of the O VI and Ne VIII. To predict column densities of various ions as a function of temperature, we employ the ion fractions in collisionally ionized gas from Gnat & Sternberg (2007); we mainly assume that the gas is in collisional ionization equilibrium (CIE), but we provide some brief comments on how the results can change if the absorption arises in non-equilibrium, rapidly cooling gas. We also must make assumptions about the metallicity and total H (H I + H II) column density of the absorbing gas [$N(\text{H}_{\text{tot}})$]. The profiles of O III, O IV, O VI, and Ne VIII are all well aligned in velocity space and there is clearly some type of relationship between the Ne VIII phase and the lower ionization material, so we assume that the hot gas has the same metallicity as the photoionized gas. With that assumption, we find the gas temperature that matches

the Ne VIII/O VI ratio and adjust $N(\text{H}_{\text{tot}})$ to fit the observed columns of the metals. Table 9 lists the results of this procedure (in the CIE case) for the $v = 0$ km s $^{-1}$ components of the absorbers at $z_{\text{abs}} = 0.68381$, 0.70152, and 0.72478, including the derived temperature and $N(\text{H}_{\text{tot}})$ as well as the predicted column density of H I in the hot gas and the H I Doppler parameter.

As an example, Figure 11 shows the predicted CIE column densities of several relevant ionization stages in the $v = 0$ km s $^{-1}$ component of the Ne VIII absorber at $z_{\text{abs}} = 0.68381$. These hot-gas models have several notable features. First, all of the observed column densities, as well as upper limits on undetected species, are fully consistent with a combination of a hot-gas phase (the source of O VI and Ne VIII) and a distinct photoionized (cool) gas phase (the source of all other detected species). In the $v = 0$ km s $^{-1}$ component at $z_{\text{abs}} = 0.68381$, the Ne VIII/O VI ratio requires a gas temperature of $T = 10^{5.7}$ K. At this temperature, the predicted S V and S VI column densities from the hot gas are both below the observed upper limits. The O IV and C III columns from the hot gas are also extremely low, so we can legitimately assume that the O IV and C III absorption only arises in the cool, photoionized phase.

On the other hand, we see from Figure 11 that even though the Ne VIII-bearing gas is hot, it does contain an appreciable amount of H I (thin black line in Figure 11): the hot-gas model predicts $\log N(\text{H I}) = 13.6$ for this component at the inferred temperature and assumed metallicity. However, H I lines arising in the hot phase will also be extremely broad ($b = \sqrt{2kT/m}$) as indicated in Table 9, and this makes detection of the broad H I absorption challenging. Our COS spectrum does not cover the Ly α line at the redshifts of the Ne VIII absorbers, and the broad Ly β line predicted by the model in Figure 11 is too weak to be detected in our data. Future observations of the Ly α line could, in principle, detect the predicted broad Ly α line and thereby corroborate our hot-gas detection. Moreover, this would provide additional information – the combined analysis of b -values of low-mass and higher-mass elements constrains the non-thermal line broadening (e.g., due to turbulence) as well as the temperature (see §4.1.1 in Tripp et al. 2008). So, while we have a good estimate of the gas temperature of the hot phase of the Ne VIII absorbers, it would still be worthwhile to observe the Ly α line to obtain more insight. Absorption systems showing evidence of broad Ly α plus narrower O VI and/or Ne VIII have been identified previously (Tripp et al. 2001; Richter et al. 2004; Narayanan et al. 2010; Savage et al. 2011a,b; Narayanan et al. 2012), and analysis of well-aligned H I and O VI absorption lines indicates that non-thermal broadening is important (Tripp et al. 2008).

We do not yet have the ability to apply such an analysis to the systems in this paper, but we can at least check if the Doppler parameters that the metal lines provide are consistent with gas temperatures implied by the Ne VIII/O VI ratios. For $\log T \approx 5.7$ K, as indicated by the Ne VIII/O VI ratios in these systems, the Doppler parameters from thermal broadening are $b(\text{O VI}) = 22.7$ km s $^{-1}$ and $b(\text{Ne VIII}) = 20.6$ km s $^{-1}$. The observed Doppler parameters for all of the Ne VIII lines in these systems are in agreement with this constraint. The best

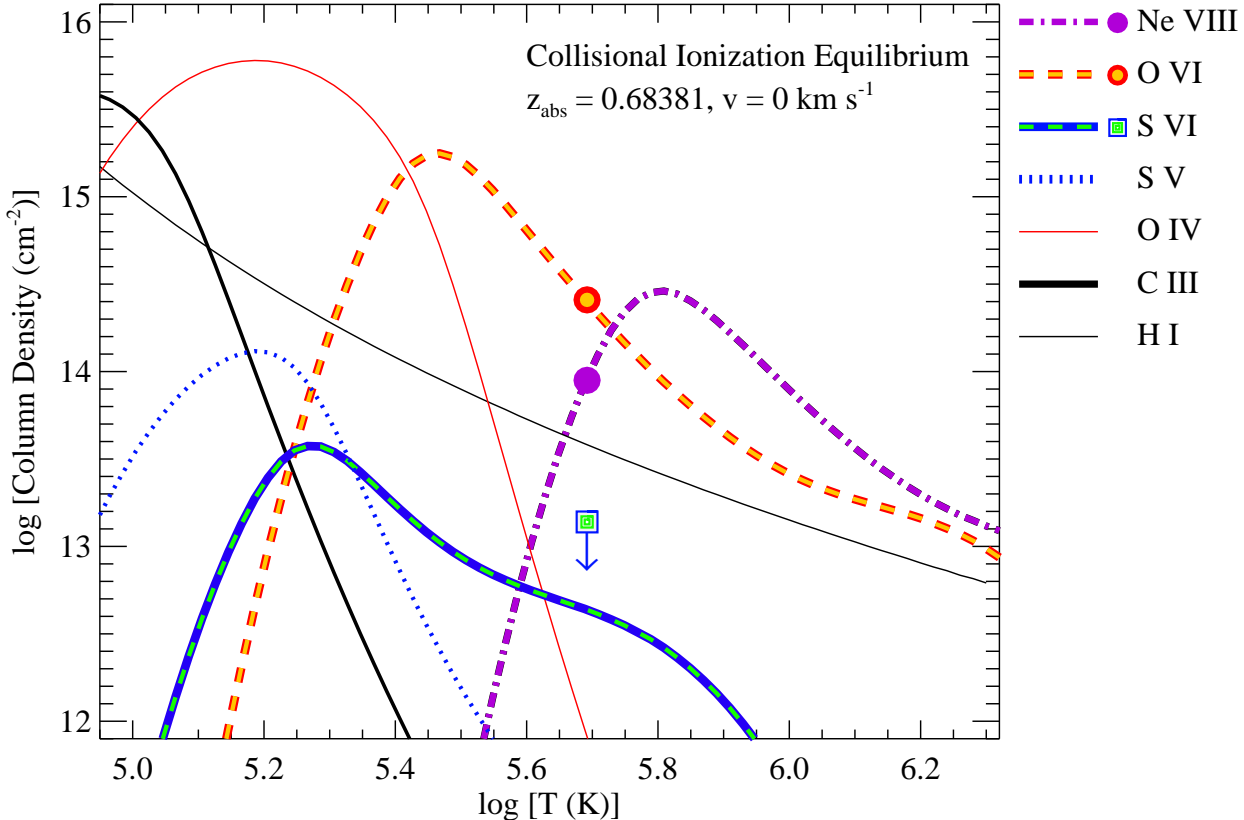


Figure 11. Collisional ionization modeling of the highly ionized species detected in the $v = 0 \text{ km s}^{-1}$ component of the PG1148+549 absorber at $z_{\text{abs}} = 0.68381$, based on the collisional ionization equilibrium ion fractions calculated by Gnat & Sternberg (2007). As in Figure 10, the column densities predicted by the model are shown with smooth curves, and the observed column densities of O VI and Ne VIII, as well as the observed 3σ upper limit on S VI, are plotted with large symbols at $T = 10^{5.7} \text{ K}$. The legend at right indicates the species that correspond to the curves and symbols.

Table 9
Properties of the Collisionally Ionized Hot Phase of the PG1148+549 Ne VIII Absorbers

Redshift	$\log [T \text{ (K)}]$	$\log [N(\text{H}_{\text{tot}}) \text{ (cm}^{-2}\text{)}]$	$\log [N(\text{H I}) \text{ (cm}^{-2}\text{)}]^{\text{a}}$	$b \text{ (km s}^{-1}\text{)}^{\text{b}}$
0.68381...	5.69	19.8	13.6	90
0.70152...	5.69	< 19.0	< 12.8	90
0.72478...	5.72	< 18.9	< 12.6	93

^a The predicted neutral hydrogen column density given the inferred temperature and $N(\text{H}_{\text{tot}})$ [see text].

^b The predicted Doppler parameter for hydrogen at the given temperature.

fit Doppler parameters for the O VI $\lambda\lambda$ 1031.93, 1037.62 lines in the $z_{\text{abs}} = 0.68381$ and $z_{\text{abs}} = 0.70152$ systems are also consistent with the expected line width. The O VI line width in the $z_{\text{abs}} = 0.72478$ system (which suffers from particularly noisy profiles) is slightly more discrepant with the expected line width but is still consistent within 2σ .

Finally, comparing the total hydrogen column densities derived for the hot gas vs. the photoionized, cool gas (compare Table 8 and 9), we see that total hydrogen column densities are generally more than an order of magnitude higher in the hot gas than in the cool gas, and therefore the hot (Ne VIII) phase likely contains substantially more mass than the photoionized gas. This is

similar to the preponderance of hot gas found by Tripp et al. (2011) in a multiphase Ne VIII absorber affiliated with a post-starburst galaxy. This conclusion rests on the assumption that the metallicity of the hot phase is roughly the same as the metallicity of the cool phase. If the hot phase has a higher metallicity, it will have a lower total hydrogen column, but we note that even if the hot phase metallicity is ten times higher than that of the cool phase, the hot gas will still harbor a similar total hydrogen column density. It has been suggested that in general, the cool circumgalactic gas detected in QSO absorbers is an important baryon reservoir (Werk et al. 2013), and it appears that there is just as much mass (or more) in the hot gas traced by Ne VIII.

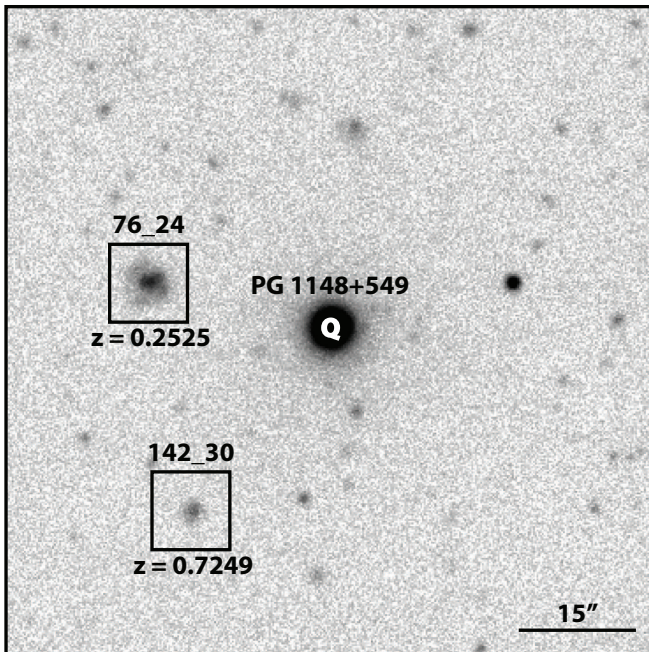


Figure 12. Deep U band image of the PG1148+549 field from the Large Binocular Telescope. The image is centered on the QSO. Galaxies for which we have obtained spectroscopic redshifts with Keck/LRIS are marked with a $10''$ box. The label above each box is our galaxy identification code; the first number in the galaxy ID label is the position angle (north through east) from in the QSO (in degrees), and the second number is the angular separation from the QSO (in arcseconds).

We have also considered the non-equilibrium collisional ionization models of Gnat & Sternberg (2007). Again, with these models we find that no single-phase model can account for the observed ratios and columns of O III, O IV, O VI, and Ne VIII – the non-equilibrium models also require a distinct, hot phase. In general, the non-equilibrium models yield pretty similar results for the hot phase but can fit the observed column densities at a slightly lower temperature (see, e.g., Figure S5 in Tripp et al. 2011). It is possible that the O VI b -value in the system at $z_{\text{abs}} = 0.72478$, which is somewhat more narrow than expected based on the CIE model, favors a non-equilibrium situation. However, higher S/N measurement of the line width is needed before this can be considered to be strong evidence.

6. AFFILIATED GALAXIES

To begin to probe the relationships between the PG1148+549 Ne VIII absorbers and nearby galaxies, we have obtained deep imaging and spectroscopy, as summarized in § 2. Figure 12 shows our U -band LBT image of the PG1148+549 field, which has a 5σ limiting magnitude of $U_{AB} = 26.0$. We obtained Keck/LRIS spectra of the four brightest objects near the sight line. The LRIS spectra showed that two of the LRIS targets are galaxies at interesting redshifts. These galaxies are labelled in Figure 12 by their position angle from the QSO (North through East) and their angular separation from the sight line. As described in Werk et al. (2012), we have estimated the star-formation rates, H II-region metallicities, absolute magnitudes, and impact parameters of the galaxies observed with LRIS. These properties are presented in Table 10, and the spectrum of galaxy 142_30 is

shown in Figure 13.

One of the LRIS galaxies (76_24) is at a low enough redshift ($z_{\text{gal}} = 0.2525$) so that we cannot check for affiliated Ne VIII, but we note that the COS spectrum shows strong O VI, C III, and multiple H I Lyman series absorption lines at this redshift, consistent with recent findings that strong O VI absorption is ubiquitous in the halos of star-forming galaxies (Prochaska et al. 2011; Tumlinson et al. 2011b). The other LRIS galaxy (142_30) is only $\Delta v \sim +30 \text{ km s}^{-1}$ from the Ne VIII absorber at $z_{\text{abs}} = 0.72478$. In many regards, Galaxy 142_30 has the characteristics one might expect to find for an object embedded in a gas-rich halo: the galaxy is luminous ($L \sim L^*$), has a high metallicity ($[\text{O}/\text{H}] = +0.22 \pm 0.15$), and a relatively high SFR of $6.42 \pm 0.44 M_{\odot} \text{ yr}^{-1}$. However, the galaxy has one surprising feature: it is fairly far from the sight line (impact parameter = 217 kpc). Given the high metallicity of the affiliated absorber, $Z > Z_{\odot}$, the relatively large distance to the nearest galaxy is notable, although we stress that more galaxy redshift measurements are required to thoroughly probe the origin of this absorbing gas.

7. DISCUSSION

7.1. Redshift Density and Baryonic Content

One of the primary goals of our COS survey is to provide some basic statistics on Ne VIII QSO absorption systems such as the number of these systems per unit redshift, dN/dz . The Ne VIII absorption lines are weak, and at the redshifts where they can be observed with *HST*, there is a moderately high density of absorption lines from other redshifts, so discovery of the Ne VIII absorbers is slow work that requires careful identification of all of the lines in a spectrum (not just the Ne VIII) to avoid spurious misidentifications. This work is underway, but we can obtain some preliminary statistics based on the PG1148+549 data.

The COS spectrum of PG1148+549 enables detection of the redshifted Ne VIII $\lambda\lambda 770.41, 780.32$ lines above $z = 0.49$. Here we are mainly interested in the circumgalactic gas in the large halos of intervening galaxies. It is known that there is a statistically significant excess of highly ionized absorbers with $z_{\text{abs}} \approx z_{\text{QSO}}$ (see, e.g., Figures 14-15 in Tripp et al. 2008), many of which arise in AGN-driven outflows and other phenomena that occur quite close to the central engine of active galactic nuclei (e.g., Ganguly & Brotherton 2008). For this reason, we excluded the region within 3000 km s^{-1} of z_{QSO} from the part of the PG1148+549 spectrum that we probed for Ne VIII absorption. Following the method outlined in Tripp et al. (2008) to account for variable S/N and regions blocked by strong lines from other redshifts, we find that the total redshift over which we can detect Ne VIII is $\Delta z = 0.43$ for a 10-pixel wide line and a minimum detection threshold of $30 \text{ m}\text{\AA}$. In terms of the comoving “absorption distance” (Bahcall & Peebles 1969),

$$dX = \frac{H_0}{H(z)}(1+z)^2 dz, \quad (1)$$

where H_0 is the Hubble constant and $H(z) = H_0 \sqrt{\Omega_m(1+z)^3 + \Omega_\Lambda}$ in our adopted cosmology, we can detect Ne VIII over a total comoving path of $\Delta X = 0.87$.

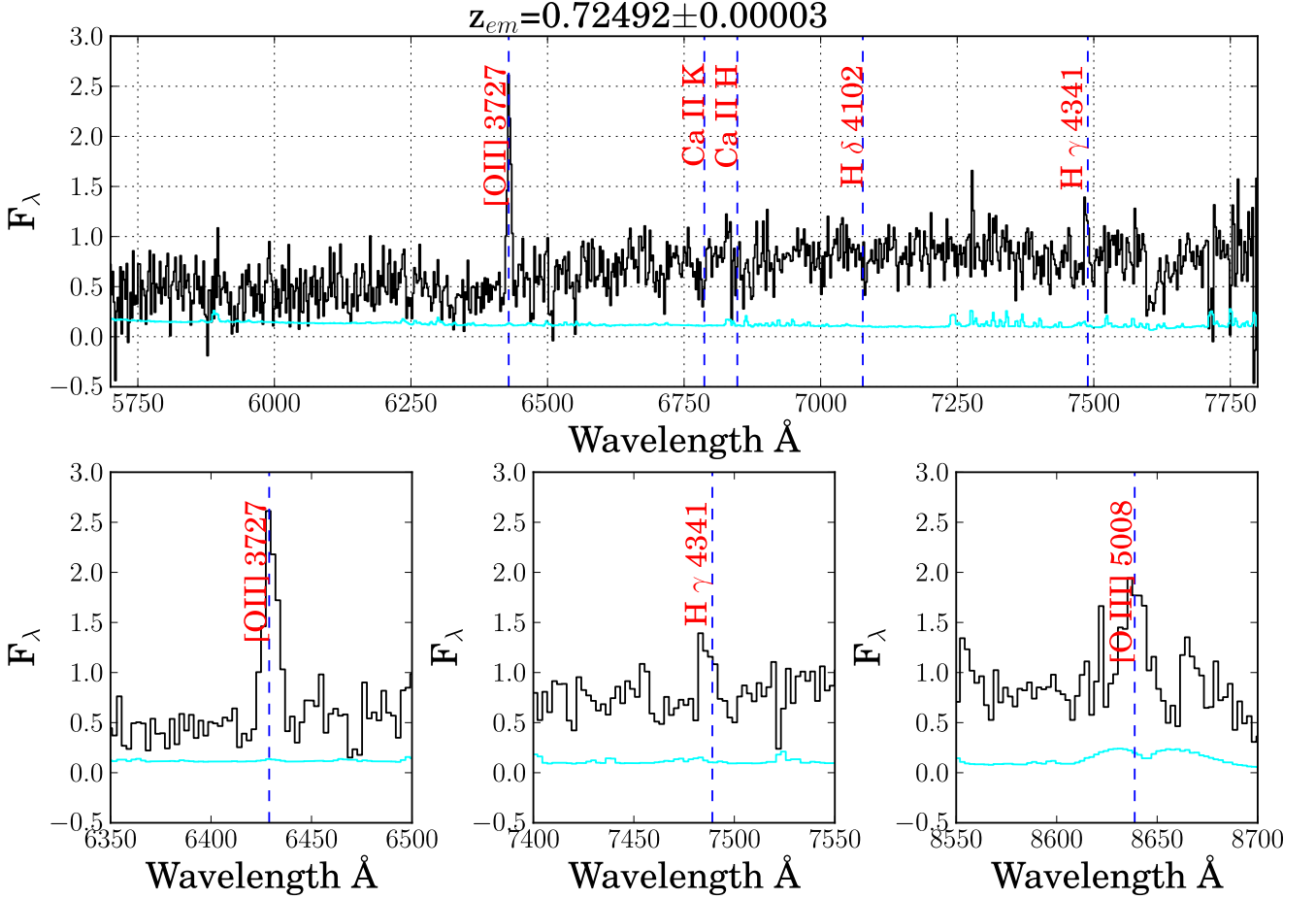


Figure 13. Keck/LRIS spectrum of the galaxy 142_30 (see Figure 12). Several emission lines are evident including Balmer lines, [O II], and [O III], and these features indicate a vacuum Heliocentric redshift of $z_{em} = 0.72492$. The emission lines also provide constraints on the star-formation rate and metallicity of the galaxy (see Table 10). The cyan line below the spectrum represents the 1σ uncertainty in the flux.

Table 10
Spectroscopic Properties of Galaxies Near PG1148+549

Galaxy ID ^a	z_{galaxy}	Impact Parameter (kpc)	Star-formation Rate ^b ($M_{\odot} \text{ yr}^{-1}$)	M_R^c	[O/H] ^b
76_24.....	0.25250	95	1.53 ± 0.04	-19.86 ± 0.04	-0.11 ± 0.15
142_30.....	0.72492	217	6.42 ± 0.44	-21.15 ± 0.13	$+0.22 \pm 0.15$

^a The first number in the galaxy identifier is the position angle (north through east) in degrees, and the second number is the angular separation from the QSO in arcseconds.

^b Star-formation rate and logarithmic metallicity measured as described in Werk et al. (2012).

^c R -band absolute magnitude.

With these numbers, we obtain $dN/dz = 7_{-4}^{+7}$ for Ne VIII absorbers with $W_0 > 30 \text{ m}\text{\AA}$ or, in terms of the comoving path, $dN/dX = 3_{-1}^{+4}$, with uncertainties from Poisson statistics (Gehrels 1986). This estimate will be revised in future work when all of the spectra from this program will be analyzed and presented. We note that the O VI $\lambda 1031.93$ lines affiliated with these Ne VIII absorbers have rest equivalent widths greater than $70 \text{ m}\text{\AA}$, and the dN/dz of O VI absorbers with $W_r > 70 \text{ m}\text{\AA}$ (Tripp et al. 2008; Tilton et al. 2012) is similar to the dN/dz that we find for Ne VIII.

We can also estimate the cosmological mass density,

$\Omega \equiv \rho/\rho_c$, traced by the Ne VIII absorbers. The cosmological mass in the form of Ne VIII ions only is

$$\Omega_{\text{Ne VIII}} = \frac{H_0 m_{\text{Ne}} \sum_i N_i(\text{Ne VIII})}{c \rho_c \Delta X} \quad (2)$$

where m_{Ne} is the mass of neon and ρ_c is the critical density. Summing over the Ne VIII absorbers discussed above, we obtain

$$\Omega_{\text{Ne VIII}} \approx 6 \times 10^{-8}.$$

The mass in Ne VIII ions is tiny, but for some questions, this quantity is a useful constraint. Most of the mass

in these absorbers is, of course, in the ionized hydrogen, which can only be estimated with models that constrain the hydrogen ionization correction. For this purpose, we use the hot-gas results presented in Table 9, and we calculate the total baryonic mass in the Ne VIII systems using

$$\Omega_b = \frac{H_0 \mu m_H \sum_i N_i(H_{tot})}{c \rho_c \Delta X}, \quad (3)$$

where m_H is the hydrogen mass and we assume $\mu = 1.3$ to account for mass in helium. From the total hydrogen column densities in Table 9 and this expression we find

$$\Omega_b \lesssim 0.002.$$

This is an upper limit because two of the Ne VIII systems provide only upper limits on $N(\text{H I})$ and $N(\text{H}_{tot})$. It is interesting to note that this upper limit amounts to $\approx 4\%$ of the baryons (Spergel et al. 2007), but we emphasize that both $\Omega_{\text{Ne VIII}}$ and Ω_b are still quite uncertain due to the small sample and uncertainty in the metallicity¹³ of the Ne VIII-bearing gas. We will revisit these quantities in a future paper when our full sample has been analyzed.

In addition to the large uncertainty due to the small sample, we note one curious aspect of the PG1148+549 Ne VIII absorbers: while our data have sufficient signal-to-noise to detect these lines over a large redshift range ($0.51 \leq z \leq 0.96$), all of the Ne VIII systems that we identify are clustered in a small portion of this redshift window with $0.68381 \leq z_{\text{abs}} \leq 0.72478$. This raises a question: could the three absorption systems be related somehow? For example, could these absorbers all be ejecta from a single galaxy? This seems unlikely because the absorber redshifts are spread over a large velocity range (7200 km s^{-1}). Outflows driven by quasars (e.g., broad absorption-line outflows) do attain such velocities, but usually these outflows exhibit many adjacent components spread over the velocity range, or they show a smooth but very broad absorption trough extending over a large velocity interval (see, e.g., Capellupo et al. 2012). The PG1148+549 Ne VIII absorbers have no resemblance to BAL outflows. Some quasars have been shown to have absorption systems due to QSO ejecta that are highly displaced in redshift from the QSO (e.g., Jannuzi et al. 1996; Bowen et al. 2001; Rodríguez Hidalgo et al. 2011), but these also show distinctive characteristics (e.g., relatively broad and smooth absorption profiles) that do not match the PG1148+549 NeVIII systems.

It seems improbable that these Ne VIII absorbers originate in an outflow from a single galaxy. A more plausible explanation is that the sight line passes through a region with a relatively high density of gas-rich, star-forming galaxies at $z \approx 0.7$, and each of the three absorbers originate from separate galaxies. This is a testable hypothesis, and we are obtaining additional deep, multi-object spectroscopy of a large number of galaxies in the

PG1148+549 field which could reveal such a large-scale structure. This spectroscopic survey is underway but not yet complete; once this has been completed, we will reexamine the origins of these Ne VIII systems. The existence of such a structure on this line of sight could bias the redshift density and baryonic content estimates. Incorporation of a larger number of sight lines is necessary to reduce the effects of this type of cosmic variance, and analysis of these statistics with larger numbers of sight lines is underway.

7.2. Cross Section, Size, and Stability

The redshift density (dN/dz) of the Ne VIII absorbers can be interpreted in a variety of ways. Frequently, dN/dz is used to estimate an effective cross section (πR^2) of absorption systems:

$$\frac{dN}{dz} = n_{\text{abs}} \pi R^2 \frac{c}{H(z)} (1+z)^2, \quad (4)$$

where n_{abs} is the spatial (volume) density (number per Mpc) of the absorbing entities (not the particle density). While we have an approximate determination of the product of n_{abs} and πR^2 , we do not know the values of these quantities individually. Nevertheless, we have derived constraints on the thickness of the low-ionization component of the absorbers (final column of Table 8) – the photoionization models imply that the low-ionization phase has a thickness ranging from less than 100 pc up to 3.5 kpc. It is important to note that all of the intervening Ne VIII absorbers in the PG1148+549 sight line and all of the Ne VIII absorbers from other sight lines reported in the literature show well detected lower ionization absorption lines that are well aligned with the Ne VIII. Therefore, it appears that the cross section of the Ne VIII and the lower ionization stages are the same – in order to detect Ne VIII, it has (so far) always been necessary for the sight line to pierce the lower ionization cloud as well. If we assume, based on the sizes derived for the lower ionization phases, that the clouds have a typical diameter of 1 kpc and we solve equation 4 for the space density, we find that $n_{\text{abs}} \approx 1100 \text{ Mpc}^{-3}$. This number is highly uncertain; just considering the 1σ uncertainty in dN/dz , n_{abs} could range from ≈ 500 up to 2000 Mpc^{-3} . Nevertheless, even with these uncertainties, n_{abs} for these absorbers is vastly larger than the space density of galaxies at $z \approx 0.7$. Integrating the galaxy luminosity functions from the DEEP2 or VVDS surveys (Willmer et al. 2006; Ilbert et al. 2005) indicates that galaxies with $L \gtrsim 0.1L_*$ have a space density of $n \approx 10^{-2}$ at this redshift. Previous studies provide strong evidence that O VI absorbers are affiliated with galaxies (Stocke et al. 2006; Prochaska et al. 2011; Tumlinson et al. 2011b), but their statistics require $> 10^4$ analogous clouds per galaxy to explain the observed dN/dz . This requirement for a large number of clouds per galaxy has been noted for other types of QSO absorbers including weak Mg II systems at similar redshifts (Rigby et al. 2002) and metal-rich C IV absorbers at higher redshifts (Schaye et al. 2007). An important caveat in this calculation is that the density of the photoionized gas, and hence the absorber thickness, depends on the assumed intensity of the photoionizing flux. While models of the UV background and observa-

¹³ The $N(\text{H}_{tot})$ derived from the models depends on the adopted metallicity of the Ne VIII-bearing gas, which we have assumed is the same as the well constrained cooler, photoionized gas in each absorber. If the Ne VIII phase tends to be more mixed with lower metallicity ambient gas, then the metallicity of the Ne VIII could be lower, which would increase $N(\text{H}_{tot})$ and Ω_b . Conversely, if the hot gas (including the Ne VIII) tends to separate from the cooler gas (as occurs in some models, e.g., Mac Low & Ferrara 1999), then the Ne VIII gas could have higher metallicity.

tional constraints on its intensity appear to be in broad agreement (see, e.g., Figure 7 in Davé & Tripp 2001), it is possible that there is substantial spatial variability of the UV background flux or systematic errors in its estimation, and this could affect our estimate of n_{abs} . Indeed, detection of Ne VIII may introduce a bias if these absorbers are more likely to arise in regions of elevated flux. However, even with this uncertainty, it seems likely that any plausible UV ionizing flux will require $n_{\text{abs}} \gg n_{\text{gal}}$.

Alternatively, we can turn this around and ask: if the Ne VIII absorbers are affiliated with some type of galaxy of known spatial density n_{gal} , what is the effective cross section of the Ne VIII-bearing gas that produces the observed dN/dz ? Tumlinson & Fang (2005) used this argument to show that if low- z O VI absorbers originate in faint/dwarf galaxies, then metals must be transported to distances of ≈ 200 kpc from their galaxies of origin (if these metals come from L^* galaxies, they must be transported even farther). As noted above, galaxies with $L \gtrsim 0.1L^*$ have a spatial density of $n_{\text{gal}} \approx 10^{-2}$ Mpc $^{-3}$ at $z = 0.7$. Equating this value of n_{gal} to n_{abs} in equation 4, we obtain $R \sim 100 - 200$ kpc, where the range reflects the uncertainty in dN/dz . Here we have assumed that the covering fraction of the Ne VIII systems is ≈ 1 ; if the covering fraction is smaller, then the effective cross section must be even larger. While this is a rough initial estimate, this implies a large transport distance for such metal-rich gas. How is solar-metallicity gas propagated to such a large distance? We note that the frequency of Ne VIII absorbers may indicate that they are more likely to be connected with lower luminosity dwarf galaxies, based on an argument analogous to the one applied by Tumlinson & Fang (2005) to the O VI systems: if the Ne VIII absorbers originate in L^* galaxies, then they must have very large effective cross sections that seem improbable. If we only consider galaxies with $L \gtrsim 1.0L^*$, for example, then the galaxy density drops to $n_{\text{gal}} \approx 10^{-3}$, which requires an effective cross section $\gtrsim 1$ Mpc. The finding of Mulchaey & Chen (2009) and Chen & Mulchaey (2009) that lower redshift Ne VIII absorbers are affiliated with sub- L^* galaxies supports this implication of the statistics.

The arguments above suggest that the Ne VIII systems arise in extended gaseous halos that are filled with a large number of small clouds. Would such a configuration be stable? For the photoionized portions of the absorbers, we can estimate the radial size of the photoionized phase, assuming it is in hydrostatic equilibrium, given the gas temperature, $N(\text{H I})$, the fraction of the mass in gas, and the H I photoionization rate (see equation 12 in Schaye 2001). Assuming typical values for these parameters, we find that the properties of the photoionized gas in Table 8 imply that the radial size of the photoionized material at $z_{\text{abs}} = 0.68381$ should be roughly 60 – 100 kpc if it is in hydrostatic equilibrium. For the systems at $z_{\text{abs}} = 0.70152$ and 0.72478, we find that similarly large clouds are expected in hydrostatic equilibrium with sizes $\gtrsim 100$ kpc. In contrast, the photoionization models suggest that the absorbers are vastly smaller (last column in Table 8).¹⁴ This might indicate that the photoionized clouds in this system are *not* in hydrostatic equilibrium

but rather are in the process of expanding and/or evaporating.

Alternatively, they could be pressure-confined by the surrounding medium. The CLOUDY models indicate that the pressure in the cool, photoionized phase is $p/k \approx 10$ cm $^{-3}$ K. If the Ne VIII phase surrounds and pressure confines the cool gas, then pressure balance requires a particle density of $\approx 10^{-5}$ cm $^{-3}$. While this is a reasonable density for halo gas, it may require sizes that are unreasonably large when combined with $N(\text{H}_{\text{tot}})$ for the hot gas (see Table 9), and for this reason it is unlikely that the Ne VIII phase pressure confines the cool gas. This is not surprising – the close alignment of the Ne VIII phase with the cooler gas suggests that the Ne VIII arises in an interface between the cool gas and a hotter (unseen) ambient medium; this hypothesis has been favored in analyses of other Ne VIII systems as well (Mulchaey & Chen 2009; Narayanan et al. 2011; Tripp et al. 2011). In this scenario, the absorber is likely not a stable entity but rather is in the process of dissipating into the halo in which it is embedded, e.g., outflow ejecta that is expanding as it moves away from its source.

8. SUMMARY

Using a high signal-to-noise spectrum of the bright QSO PG1148+549 ($z_{\text{QSO}} = 0.9754$) obtained with the Cosmic Origins Spectrograph, we have discovered three new Ne VIII absorption-line systems at redshifts ranging from $z_{\text{abs}} = 0.68381$ to 0.72478. These absorbers exhibit a variety of absorption lines from other metals including C III, N IV, O III, O IV, and O VI. In this work we have reported on the physical conditions and ionization of these multiphase Ne VIII/O VI absorbers, and we have discussed the implications of measurements regarding the nature and origin of the absorbers. In summary, our primary conclusions are the following:

1. A single-phase model in which all of the ions are produced via photoionization or collisional ionization fails to reproduce the observed column density ratios; a multiphase absorption system is clearly required to explain the range of detected ions (from O III up to Ne VIII). Moreover, the O VI and Ne VIII cannot originate in photoionized plasma – models in which the high ions are produced via photoionization predict unphysically large cloud sizes, with absorption lines that would be highly spread out by broadening in the Hubble flow. We conclude that the O VI and Ne VIII lines arise in collisionally ionized gas with $T \sim 10^{5.7}$ K, while the low ions are produced via photoionization.
2. The oxygen abundances of the systems, as determined from the low ions and photoionization modeling, are all $[\text{O}/\text{H}] > -0.5$, higher than the typically assumed metallicity of the CGM/IGM of $[\text{X}/\text{H}] \sim -1.0$. The $z_{\text{abs}}=0.70152$ and $z_{\text{abs}}=0.72478$ systems require supersolar metallicities. These are abundances in the cool gas, and we assume for our analysis that the hot gas probed by the Ne VIII

ground from quasars. A local ionizing source, which would cause the ionizing photon density to be higher, would require higher particle densities and even smaller clouds, so this would only exacerbate the discrepancy.

¹⁴ The particle densities and absorber thicknesses in Table 8 were derived assuming the absorber is ionized by the diffuse UV back-

has a similar metallicity. The hot gas could have a different metallicity than the cool phase, e.g., it could be more metal rich because hot gas tends to separate from the cooler material in outflows (e.g., Mac Low & Ferrara 1999). On the other hand, the metallicity of the major baryon reservoirs in the CGM and IGM may have much lower metallicities and we are not yet detecting those reservoirs; detection of such low-metallicity material in metal absorption lines may require significantly higher signal-to-noise spectroscopy.

3. The absorbers also indicate moderate underabundances of carbon and nitrogen (compared to oxygen) at a level similar to the C and N underabundances observed in Milky Way halo stars.
4. Assuming that a portion of the gas is photoionized by the UV background from quasars and galaxies, the ionization models indicate that the low-ionization phase has low density ($\approx 10^{-4} \text{ cm}^{-3}$), small size (3.5 kpc down to $< 100 \text{ pc}$), and low thermal pressure, $p/k \approx 10 \text{ cm}^{-3} \text{ K}$. The total (H I + H II) hydrogen column densities in these absorbers ranges from $< 10^{17.1} \text{ cm}^{-2}$ up to $10^{18.5} \text{ cm}^{-2}$.
5. The hot, collisionally ionized phase that contains O VI and Ne VIII has $T \approx 10^{5.7} \text{ K}$ based on the O VI to Ne VIII ratio, assuming collisional ionization equilibrium. Non-equilibrium models (Gnat & Sternberg 2007) require only slightly lower temperatures. The ionization models indicate that the total hydrogen column density in the hot gas is approximately $10\times$ higher than the total hydrogen column in the cool, photoionized material.
6. The COS spectrum has sufficient S/N to reveal Ne VIII lines with $W_r > 30 \text{ m}\text{\AA}$ over a total redshift window of $\Delta z = 0.43$ (or a comoving absorption distance $\Delta X = 0.87$), which implies a redshift density of $dN/dz = 7_{-4}^{+7}$ (comoving redshift density $dN/dX = 3_{-1}^{+4}$). The cosmological mass density of the Ne VIII ions is $\Omega_{\text{Ne VIII}} \approx 6 \times 10^{-8}$, and a preliminary constraint on the baryon mass in these absorbers is $\Omega_b \lesssim 0.002$.
7. Given the small sizes implied for the low-ionization phase that is always detected along with the Ne VIII, the observed dN/dz indicates that galaxies generally have a large number of these metal-enriched, multiphase clouds in their halos with effective cross sections of 100 kpc or more.
8. However, the clouds are unlikely to be stable and long-lived. The small size of the photoionized phase implies that the clouds will expand and dissipate, and the correlation of the Ne VIII phase with the photoionized phase suggests that the Ne VIII is the transitional layer produced as the cool gas is heated and photoionized, ultimately destined to blend into the hotter ambient halo of the circumgalactic medium.

ACKNOWLEDGMENTS

We thank Hsiao-Wen Chen for comments on the manuscript, and we thank Christina Williams and Marcel Neeleman for technical assistance. This research

was supported by NASA grants HST-GO-11741 and NNX08AJ44G. J.X.P. also appreciates support from NSF grant AST-0709235. The W. M. Keck Observatory is operated as a scientific partnership between the California Institute of Technology, the University of California, and the National Aeronautics and Space Administration. The Keck Observatory was made possible by the generous financial support of the W. M. Keck Foundation. The authors wish to recognize and acknowledge the very significant cultural role and reverence that the summit of Mauna Kea has always had within the indigenous Hawaiian community. We are most fortunate to have the opportunity to conduct observations from this mountain. This work also made use of data from the Large Binocular Telescope. The LBT is an international collaboration among institutions in the United States, Italy, and Germany. The LBT Corporation partners are: The University of Arizona on behalf of the Arizona university system; Istituto Nazionale di Astrofisica, Italy; LBT Beteiligungsgesellschaft, Germany, representing the Max Planck Society, the Astrophysical Institute Potsdam, and Heidelberg University; The Ohio State University; The Research Corporation, on behalf of The University of Notre Dame, University of Minnesota, and University of Virginia.

REFERENCES

- Akerman C.J., Carigi L., Nissen P.E., Pettini M., Asplund M., 2004, *A&A*, 414, 931
- Anderson M.E., Bregman J.N., 2010, *ApJ*, 714, 320
- Aracil, B., Tripp, T. M., Bowen, D. V., Prochaska, J. X., Chen, H.-W., & Frye, B. L. 2006, *MNRAS*, 367, 139
- Asplund M., Grevesse N., Sauval A.J., Scott P., 2009, *ARA&A*, 47, 481
- Bahcall, J. N., & Peebles, P. J. E., 1969, *ApJ*, 156, L7
- Bechtold, J., Dobrzycki, A., Wilden, B., Morita, M., Scott, J., Dobrzycka, D., Tran, K.-V., & Aldcroft, T. L., 2002, *ApJS*, 140, 143
- Bell, E. F., McIntosh, D. H., Katz, N., & Weinberg, M. D., 2003, *ApJ*, 585, L117
- Bensby, T., & Feltzing, S. 2006, *MNRAS*, 367, 1181
- Bouché, N., Dekel, A., Genzel, R. et al. 2010, *ApJ*, 718, 1001
- Bowen D.V., et al., 2008, *ApJS*, 176, 59
- Bowen, D. V., Jimenez, R., Jenkins, E. B., & Pettini, M., 2001, *ApJ*, 547, 39
- Brady Ford, A., Oppenheimer, B. D., Davé, R., Katz, N., Kollmeier, J. A., & Weinberg, D. H., 2012, *MNRAS*, submitted (arXiv 1206.1859)
- Brooks, A. M., Governato, F., Quinn, T., Brook, C. B., & Wadsley, J., 2009, *ApJ*, 694, 396
- Capellupo, D. M., Hamann, F., Shields, J. C., Rodríguez Hidalgo, P., & Barlow, T. A., 2012, *MNRAS*, 422, 3249
- Cen R., Tripp T. M., Ostriker J. P., Jenkins E. B. 2001, *ApJ*, 559, L5
- Cen R., Fang T., 2006, *ApJ*, 650, 573
- Cen R., Chisari N. E., 2011, *ApJ*, 731, 11
- Chen, H.-W., & Mulchaey, J. S., 2009, *ApJ*, 701, 1219
- Chen H.-W., & Prochaska J.X., 2000, *ApJ*, 543, 9
- Churchill, C. W., Kacprzak, G. G., Steidel, C. C., Spitler, L. R., Holtzman, J., Nielsen, N. M., Trujillo-Gomez, S., 2012, *ApJ*, 760, 68
- Cooke, R., Pettini, M., & Murphy, M. T., 2012, *MNRAS*, 425, 347
- Cooke, R., Pettini, M., Steidel, C. C., Rudie, G. C., & Nissen, P. E., 2011, *MNRAS*, 417, 1534
- Davé, R., et al. 2001, *ApJ*, 552, 473
- Davé, R., & Tripp, T. M., 2001, *ApJ*, 553, 528
- Dekel, A., & Birnboim, Y., 2006, *MNRAS*, 368, 2
- Dekel, A., & Silk, J., 1986, *ApJ*, 303, 39
- Fabbian, D., Nissen, P. E., Asplund, M., Pettini, M., & Akerman, C., 2009, *A&A*, 500, 1143

- Fang T., Bryan G. L. 2001, *ApJ*, 561, L31
- Ferland G. J., Korista K.T., Verner D.A., Ferguson J.W., Kingdon J.B., Verner E.M., 1998, *PASP*, 110, 761
- Fox, A. J., Wakker, B. P., Savage, B. D., Tripp, T. M., Sembach, K. R., & Bland-Hawthorn, J., 2005, *ApJ*, 630, 332
- Froning C.S., Green J.C., *Ap&SS*, 320, 181
- Fukugita M., Hogan C.J., Peebles P.J.E., 1998, *ApJ*, 503, 518
- Fumagalli, M., Prochaska, J. X., Kasen, D., Dekel, A., Ceverino, d., & Primack, J. R., 2011, *MNRAS*, 418, 1796
- Ganguly, R., & Brotherton, M. S., 2008, *ApJ*, 672, 102
- Ganguly, R., Cen, R., Fang, T., & Sembach, K., 2008, *ApJ*, 678, 89
- Ganguly, R., Sembach, K. R., Tripp, T. M., Savage, B. D., & Wakker, B. P., 2006, *ApJ*, 645, 868
- Gehrels N., 1986, *ApJ*, 303, 336
- Ghavamian, P., et al. 2009, Preliminary Characterization of the Post-Launch Line Spread Function of COS, <http://www.stsci.edu/hst/cos/documents/isrs/>
- Giallongo, E., Ragazzoni, R., Grazian, A. et al. 2008, *A&A*, 482, 349
- Giallisco, M., Vanzella, E., Salimbeni, S., et al., 2011, *ApJ*, 743, 95
- Gilli, R., Comastri, A., & Hasinger, G. 2007, *A&A*, 463, 79
- Gnat O., Sternberg A., 2007, *ApJS*, 168, 213
- Green J. C., Froning, C. S., Osterman, S., et al., 2012, *ApJ*, 744, 60
- Haardt F., Madau P., 1996, *ApJ*, 461, 20
- Haardt F., Madau P., in 21st Moriond Astrophysics Meeting, Clusters of Galaxies and the High Redshift Universe Observed in X-rays, Recent Results of XMM-Newton and Chandra, ed. D. M. Neumann, J. T. T. Van
- Haardt, F., & Madau, P., 2012, *ApJ*, 746, 125
- Hamann, F. 1997, *ApJS*, 109, 279
- Hamann, F., Cohen, R. D., Shields, J. C., Burbidge, E. M., Junkkarinen, V., & Crenshaw, D. M., 1998, *ApJ*, 496, 761
- Heckman T.M., Dahlem M., Lehnert M.D., Fabbiano G., Gilmore D., Waller W.H., 1995, *ApJ*, 448, 98
- Howk J.C., Ribaudo J.S., Lehner N., Prochaska J., Chen H-W., 2009, *MNRAS*, 396, 1875
- Howk, J. C., Sembach, K. R., Savage, B. D., Massa, D., Friedman, S. D., & Fullerton, A., 2002, *ApJ*, 569, 214
- Ilbert O., et al., 2005, *A&A*, 2005, 439, 863
- Jannuzi, B. T., Hartig, G. F., Kirhakos, S. et al. 1996, *ApJ*, 470, 11
- Jenkins, E. B., 1978, *ApJ*, 219, 845
- Jenkins, E. B., 1996, *ApJ*, 471, 292
- Kacprzak, G. C., Churchill, C. W., Steidel, C. C., Spitler, L. R., & Holtzman, J. A., 2012, *MNRAS*, 427, 3029
- Kereš, D., Katz, N., Davé, R., Fardal, M., & Weinberg, D. H., 2009, *MNRAS*, 396, 2332
- Kereš, D., Katz, N., Weinberg, D. H., & Davé, R., 2005, *MNRAS*, 363, 2
- Kwak K., Henley D.B., Shelton R.L., 2011, *ApJ*, 739, 30
- Larson, R. B., 1972, 236, 21
- Lehner, N., Howk, J. C., Tripp, T. M., et al. 2013, *ApJ*, submitted (arXiv 1302.5424)
- Lehner N., et al., 2009, *ApJ*, 694, 734
- Li J.-T., Li Z., Wang Q.D., Irwin J. A., Rossa J., 2008, *MNRAS*, 390, 59
- Lodders, K., 2003, *ApJ*, 591, 1220
- Mac Low, M.-M., & Ferrara, A. 1999, *ApJ*, 513, 142
- Maller A.H., Bullock J.S., 2004, *MNRAS*, 35, 694
- Martin C.L., Kobulnicky H.A., T.M., 2002, *ApJ*, 574, 663
- Meiring J.D., Tripp T.M., Prochaska J.X., Tumlinson J., Werk J., Jenkins E.B., Thom C., O'Meara J.M., Sembach K.R., 2011, *ApJ*, 732, 35
- Misawa, T., Charlton, J. C., Kobulnicky, H. A., Wakker, B. P., & Bland-Hawthorn, J. 2009, *ApJ*, 695, 1382
- Mulchaey, J. S., & Chen, H.-W., 2009, *ApJ*, 698, L46
- Murray, N., Ménard, B., & Thompson, T. A., 2011, *ApJ*, 735, 66
- Mushotzky, R. F., Cowie, L. L., Barger, A. J., & Arnaud, K. A., 2000, *Nature*, 404, 459
- Muzahid, S., Srianand, R., Savage, B. D., Narayanan, A., Mohan, V., & Dewangan, G. C., 2012, *MNRAS*, 424, 59
- Muzahid, S., Srianand, R., Arav, N., Savage, B. D., & Narayanan, A. 2013, *MNRAS*, submitted (arXiv 1302.5510)
- Narayanan, A., Savage, B. D., Wakker, B. P., et al., 2011, *ApJ*, 730, 15
- Narayanan, A., Savage, B. D., & Wakker, B. P., 2012, *ApJ*, 752, 65
- Narayanan A., Wakker B. P., Savage B. D. 2009, *ApJ*, 703, 74
- Narayanan A., Wakker B. P., Savage B. D., Keeney, B. A., Shull, J. M., Stocke, J. T., & Sembach, K. R., 2010, *ApJ*, 721, 960
- O'Meara J. M., Burles S., Prochaska J. X., Prochter G. E., Bernstein R. A., Burgess K. M., 2006, *ApJ*, 649, L61
- Oppenheimer B.D., Davé R., 2006, *MNRAS*, 373, 1265
- Oppenheimer B.D., Davé R., 2009, *MNRAS*, 395, 1875
- Oppenheimer B.D., Davé R., Katz N., Kollmeier J.A., Weinberg D.H., 2011, *MNRAS*, in press
- PAgel B.E.J., Edmunds M.G., 1981, *ARAA*, 19, 77
- Penprase, B. E., Prochaska, J. X., Sargent, W. L. W., Toro-Martinez, I., & Beeler, D. J. 2010, *ApJ*, 721, 1
- Persic, M., & Salucci, P., 1992, *MNRAS*, 258, 14P
- Petitjean, P., & Srianand, R., 1999, *A&A*, 345, 73
- Pettini, M., & Cooke, R. 2012, *MNRAS*, 425, 2477
- Pettini M., Zych B.J., Steidel C.C., Chaffee F.H., 2008, *MNRAS*, 385, 2011
- Prochaska J.X., Weiner B., Chen H.-W., Mulchaey J., Cooksey K., 2011, *ApJ*, 740, 91
- Rauch, M., Miralda-Escudé, J., Sargent, W. L. W., et al. 1997, *ApJ*, 489, 7
- Ribaudo, J., Lehner, N., Howk, J. C., Werk, J. K., Tripp, T. M., Prochaska, J. X., Meiring, J. D., & Tumlinson, J., 2011, *ApJ*, 743, 207
- Richter, P., Savage, B. D., Tripp, T. M., & Sembach, K. R., 2004, *ApJS*, 153, 165
- Rigby, J. R., Charlton, J. C., & Churchill, C. W., 2002, *ApJ*, 565, 743
- Rodríguez Hidalgo, P., Hamann, F., & Hall, P., 2011, *MNRAS*, 411, 247
- Savage B.D., Sembach K.R., 1991, *ApJ*, 151, 313
- Savage B. D., Lehner N., Wakker B. P., Sembach K. R., Tripp T. M. 2005, *ApJ*, 626, 776
- Savage, B. D., & Lehner, N., 2006, *ApJS*, 162, 134
- Savage, B. D., Lehner, N., & Narayanan, A., 2011, *ApJ*, 743, 180
- Savage B. D., Narayanan A., Lenher N., Wakker B.P., 2011, *ApJ*, 731, 14
- Schaye J., 2001, *ApJ*, 559, 507
- Schaye J., Carswell R.F., Kim T.-S., 2007, *MNRAS*, 379, 1169
- Sembach, K. R., & Savage, B. D., 1992, *ApJS*, 83, 147
- Sembach, K. R., Wakker, B. P., Savage, B. D., et al. 2003, *ApJS*, 146, 165
- Smith, B. D., Hallman, E. J., Shull, J. M., & O'Shea, B. W., 2011, *ApJ*, 731, 6
- Spergel D.N., Bean R., Dore O., Nolte M.R., Bennett C.L., Dunkley J., Hinshaw G., Jarosik N., Komatsu E., Page L., 2007, *ApJS*, 170, 377
- Springel, V., & Hernquist, L., 2003, *MNRAS*, 339, 289
- Steidel, C. C., Erb, D. K., Shapley, A. E., Pettini, M., Reddy, N., Bogosavljević, M., Rudie, G. C., & Rakic, O., 2010, *ApJ*, 717, 289
- Stewart, K. R., Kaufmann, T., Bullock, J. S., Barton, E. J., Maller, A. H., Diemand, J., & Wadsley, J., 2011, *ApJ*, 738, 39
- Stinson, G. S., Brook, C., Prochaska, J. X., et al. 2012, *MNRAS*, 425, 1270
- Stocke, J. T., Keeney, B. A., Danforth, C. W., et al. 2013, *ApJ*, 763, 148
- Stocke, J. T., Penton, S. V., Danforth, C. W., Shull, J. M., Tumlinson, J., & McLin, K. M., 2006, *ApJ*, 641, 217
- Tepper-García T., Richter P., Schaye J., Booth C.M., Vecchia C.D., Theuns T., Wiersma R.P.C., 2011, *MNRAS*, 413, 190
- Thom, C., Tumlinson, J., Werk, J. K., et al. 2012, *ApJ*, 758, L41
- Thom, C., Werk J.E., Tumlinson J., Prochaska J.X., Meiring J.D., Tripp T.M., Sembach K.R., 2011, *ApJ*, 736, 1
- Tilton, E. M., Danforth, C. W., Shull, J. M., & Ross, T. L., 2012, *ApJ*, 759, 112
- Tinsley B.M., 1975, *ApJ* 197, 159
- Tosi, M., 1988, *A&A*, 197, 47
- Tremonti, C. A., Moustakas, J., & Diamond-Stanic, A. M., 2007, *ApJ*, 663, L77
- Tripp, T. M., Aracil, B., Bowen, D. V., & Jenkins, E. B. 2006, *ApJ*, 643, L77

- Tripp, T. M., Giroux, M. L., Stocke, J. T., Tumlinson, J., & Oegerle, W. R., 2001, *ApJ*, 563, 724
- Tripp, T. M., Jenkins, E. B., Bowen, D. V., Prochaska, J. X., Aracil, B., & Ganguly, R. 2005, *ApJ*, 619, 714
- Tripp, T. M., Meiring, J. D., Prochaska, J. X. et al., 2011, *Science*, 2011, 334, 952
- Tripp, T. M., Savage, B. D., & Jenkins, E. B., 2000, *ApJ*, 534, L1
- Tripp T.M., Sembach K.R., Bowen D.V., Savage B.D., Jenkins E.B., Lehner N., Richter P., 2008, *ApJS*, 177, 39
- Trump, J. R., Hall, P. B., Reichard, T. A., et al. 2006, *ApJS*, 165, 1
- Tumlinson J.T., Fang T., 2005, 623, L97
- Tumlinson J.T., Werk J.K., Thom C.T., Meiring J.D., Prochaska J.X., Tripp T.M., Okrochkov M., Sembach K.R., 2011, 733, 111
- Tumlinson J.T., et al., 2011, *Science*, 334, 948
- Veilleux S., Cecil G., Bland-Hawthorn J., 2005, *ARAA*, 43, 769
- Verner D.A., Barthel P.D., Tytler D., 1994, *A&ASS*, 108, 287
- Wakker, B. P., Savage, B. D., 2009, *ApJS*, 182, 378
- Weinberg, D. H., Miralda-Escudé, J., Hernquist, L., & Katz, N. 1997, *ApJ*, 490, 564
- Weiner, B. J., Coil, A. L., Prochaska, J. X., et al., 2009, *ApJ*, 692, 187
- Werk J. K., Prochaska, J. X., Thom, C., Tumlinson, J., Tripp, T. M., O'Meara, J. M., & Meiring, J. D., 2012, *ApJS*, 198, 3
- Werk J. K., Prochaska, J. X., Thom, C., Tumlinson, J., Tripp, T. M., O'Meara, J. M., & Peebles, M. 2013, *ApJS*, 204, 17
- White, S. D. M., & Rees, M. J., 1978, *MNRAS*, 183, 341
- Willmer, C. N. A., Faber, S. M., Koo, D. C. et al., 2006, *ApJ*, 647, 853
- Worthey G., Dorman B., Jones L.A., 1996, *AJ*, 112, 948
- van den Bergh, S., 1962, *AJ*, 67, 486